Rapid optimization of stationary tokamak plasmas in RAPTOR: demonstration for the ITER hybrid scenario with neural network surrogate transport model QLKNN

S Van Mulders[1], F Felici[1], O Sauter[1], J Citrin[2], A Ho[2], M Marin[2] and K L van de Plassche[2]

[1] Ecole Polytechnique Fédérale de Lausanne (EPFL), Swiss Plasma Center (SPC), CH-1015 Lausanne, Switzerland

[2] Dutch Institute for Fundamental Energy Research (DIFFER), PO Box 6336, 5600 HH Eindhoven, The Netherlands

E-mail: simon.vanmulders@epfl.ch

Abstract. This work presents a fast and robust method for optimizing the stationary radial distribution of temperature, density and parallel current density in a tokamak plasma and its application to first-principle-based modeling of the ITER hybrid scenario. A new solver is implemented in the RAPTOR transport code, enabling direct evaluation of the stationary solution to which the radial plasma profiles evolve. Coupled to a neural network emulation of the quasi-linear gyrokinetic QuaLiKiz transport model (QLKNN-hyper-10D), a first-principle-based estimate of the stationary state of the core plasma can be found at unprecedented computational speed (typically a few seconds on standard hardware). The stationary state solver is then embedded in a numerical optimization scheme, allowing the optimization of tokamak plasma scenarios in only a few minutes. The proposed method is applied to investigate the performance of ITER hybrid scenarios at different values of total plasma current, plasma density and pedestal height and for different power contributions in a heating mix consisting of electron cyclotron and neutral beam heating. Optimizing the radial distribution of electron cyclotron current drive deposition, the q profile is tailored to maximize the fusion gain Q, by maximizing the energy confinement predicted through the first-principles-based transport model, while satisfying $q > 1$, avoiding sawtooth oscillations. It is found that optimal use of ECCD in ITER hybrid scenarios is to deposit power as close to the core as possible, while maintaining sufficient off-axis current drive to keep q above 1. Upper limits for the fusion gain Q are shown to be constrained either by minimum power requirements for the separatrix power flow to maintain H-mode or by minimum current drive requirements for q profile tailoring. Finally, it is shown that the ITER hybrid scenario operating window is significantly extended by an upgrade of the electron cyclotron power to 40 MW.

Submitted to: *Nucl. Fusion*

1. Introduction

A key challenge for reactor-relevant tokamak operation is the pursuit of stable, high-performance plasma regimes, maximizing core temperature and density while minimizing external heating and current drive requirements and avoiding disruptive limits. The spatial distribution of current density and ion and electron temperature and density are of paramount importance for both discharge performance and stability. Control over externally applied heating, fueling and current drive sources allows tailoring of these plasma profiles.

A hierarchy of tokamak plasma simulators with different levels of physics fidelity and different degree of integration is justified by the wide variety of applications. Fast core transport solvers (originally developed for control-oriented applications, e.g. early work in [1]) achieve real-time execution speeds for time evolution of the plasma profile dynamics, providing a valuable tool for automated discharge optimization, fast full-discharge simulation and model-based control. Routine discharge modeling prior to experiments is foreseen to become common practice on future devices like ITER [2].

From its original conception, the RAPTOR code was envisioned both as a real-time, interpretative code [3] and a predictive simulator, which can be embedded in a non-linear optimization routine [4]. The RAPTOR code has been applied for automated optimization of tokamak actuator trajectories, yielding optimal control strategies during both the ramp-up phase [4], [5] and the ramp-down phase [6] of tokamak plasma discharges, pursuing respectively successful access to and safe termination of high-performance plasmas.

Other fast simulators are being used for predictive scenario simulations. The METIS code [7] applies a mixed 0D-1D approach, relying on confinement time scaling laws. For DIII-D, in particular for advanced scenario development, a model for poloidal flux and electron temperature diffusion, also based on scaling laws, is integrated in a trajectory optimization scheme [8]. Solvers directly evaluating the stationary plasma state include the PLASMOD code [9], [10], which solves self-consistently for the MHD equilibrium with a 3-moment solver and utilizes a simple gyro-bohm model to evaluate transport, and the GOTRESS code [11], which solves solely for heat transport and features various turbulent transport models.

A distinctive feature of the RAPTOR code is the analytical evaluation of the Jacobian matrices used within the implicit time integration scheme. This allows for a numerically stable evolution of the ordinary differential equations (ODEs), even for a large time step size (stiff and non-linear system of ODEs, obtained by finite element spatial discretization of the transport equations). Furthermore, as discussed in [4], knowledge of these Jacobian matrices allows the solution of the plasma profiles sensitivity to a chosen set of parameters and the construction of linearized models of the plasma profile dynamics along the nominal state evolution. These two capabilities are highly valuable for optimization and control applications.

The application of neural networks to the prediction of turbulent heat and particle fluxes in the core of a tokamak plasma allows for fast first-principle-based modeling of plasma profiles [12], [13], providing an avenue towards application in real-time tokamak plasma control and automated scenario optimization [14]. These neural networks are non-linear multivariate regressions of turbulent fluxes obtained with quasi-linear gyrokinetic transport codes. The quasi-linear assumption provides a major speed-up compared to direct numerical simulation of turbulent fluxes within a non-linear gyrokinetic framework and allows the generation of the required large database of turbulent flux calculations. The RAPTOR code was recently coupled to QLKNN-hyper-10D [15], henceforth abbreviated to QLKNN, a surrogate turbulent core transport model. The 10-dimensional neural network was trained on a database of 3×10^8 heat and particle flux calculations of QuaLiKiz, a quasi-linear gyrokinetic transport

model described in [16], [17]. Since the database was populated by applying a hypercube-based approach, the training set covers a wide operating space, including ITER regimes. On present-day tokamaks, routine first-principle-based discharge modeling applying quasi-linear models like QuaLiKiz and TGLF is in good agreement with experimental data, hence giving confidence to use these models to predict and optimize ITER performance [18]. The resulting neural network emulation successfully captures core transport features like the stiffness of the core plasma temperature profiles (the turbulent fluxes are highly sensitive to an increase in gradient once a critical gradient is exceeded).

Coupling a transport solver to a model featuring the stiff behaviour of plasma turbulence can compromise robust convergence. Various solver schemes have been proposed to enhance numerical stability. Both in [19] and [11], spatial gradients are considered separate variables in the non-linear set of equations, which are respectively solved by application of non-linear iterative schemes or global optimization algorithms. The finite difference scheme proposed in [20] introduces an artificial diffusivity (counteracted by a pinch term) to avoid numerical oscillations around the critical gradient in time-dependent simulations. The TGYRO solver presented in [21] features a Newton's method to find the logarithmic temperature gradients driving the amount of transport set by the heat sources, from which the temperature profiles are then inferred by integration. Note that the availability of a neural network surrogate transport model aids convergence, by providing a smooth regression with cheaply available analytic Jacobians.

In this paper, the implementation of a stationary state solver in RAPTOR is discussed, along with a scheme allowing for the automated optimization of plasma scenarios. As a specific application, we apply the RAPTOR-QLKNN optimization scheme to the optimization of the shape of the q profile for the ITER hybrid scenario. This scenario achieves improved energy confinement relative to the IPB98(y,2) scaling law [22] by actively tailoring the q profile and its radial derivative, impacting the turbulent transport fluxes by altering the ion temperature gradient (ITG) threshold. QLKNN successfully captures this physics mechanism in its prediction of the ITG-driven heat flux. Various integrated modeling studies have confirmed the potential of hybrid scenarios to provide long-pulse ($t_{burn} > 1000\,\mathrm{s}$) discharges with burning plasma conditions (fusion gain $Q \geq 5$), e.g. [23], [24] and [25], although simulation results are strongly dependent on the applied heating mix and assumptions like temperature pedestal height and density peaking. The present simulations do not take into account the magnetic flux pumping effect and rely on off-axis electron cyclotron current drive to shape the q profile, to maximize confinement and maintain $q > 1$.

The obtained scenarios are, by construction, stationary and can hence be maintained throughout the burn phase. Access to these operating points is presently not discussed, although it has been demonstrated how relaxed plasma profiles can be obtained in the early flat-top phase by optimizing actuator trajectories during the ramp-up, as demonstrated in [4] and [5] with RAPTOR-based optimization and in [26] with the physics-oriented TRANSP code.

Several works, like [27] and [28] for ITER, [29] for JT-60SA and [30] for SPARC have used predictive modeling tools to explore the existence of stationary scenarios for current and future devices. The work shown in this paper has the potential to substantially reduce the effort of such modeling activities by calculating stationary states directly (without requiring iteration between several codes) and allowing the use of numerical optimization tools to find optimal scenarios satisfying constraints. These can then serve as starting point for more sophisticated analysis using more detailed physics codes.

The remainder of this paper is structured as follows: Section 2 discusses the set of non-linear diffusion equations used in RAPTOR to model core transport, including the reduced

physics models allowing fast execution speed, and the Newton-Raphson solver implemented to find their stationary solution. Section 3 presents the application of a generic framework for automated optimization of stationary plasma states (technical details are given in Appendix B). Scenario goals are defined with a cost function (e.g. fusion gain) and a set of constraints (e.g. avoiding disruptive limits or unwanted sawtooth activity), each with user-defined functional dependencies on the plasma state and the actuator inputs. Fast convergence is obtained by providing a non-linear programming optimization algorithm with analytical Jacobians, as illustrated for the case of electron cyclotron current drive deposition optimization with a simple transport model. Section 4 illustrates the application of the optimization framework to the ITER hybrid scenario. The QLKNN first-principle-based transport model enables the prediction of the ITER hybrid operational window under various assumptions. The maximum achievable fusion gain Q is compared for various values of total plasma current, heating mix contributions, pedestal height and plasma density, maximizing energy confinement and avoiding sawtooth activity by tailoring the q profile, optimizing the radial distribution of electron cyclotron current drive deposition. Conclusions are formulated in Section 5.

2. Implementation of a stationary state solver in RAPTOR

2.1. The equations governing the plasma state evolution

The RAPTOR code [3], [14] is a control-oriented core transport solver, solving the non-linear, coupled 1-dimensional partial differential equations (PDEs) governing the response of the plasma state to the applied actuator time traces. The actuated variables include the total plasma current $I_p(t)$ (in practice feedback controlled with the central solenoid) and radially distributed deposition profiles of auxiliary heating $P_{e,i\ aux}(\rho,t)$, auxiliary current drive $j_{aux}(\rho,t)$ and gas injection $S_{e,i\ fuel}(\rho,t)$), with ρ the normalized square root of the enclosed toroidal magnetic flux. The plasma state consists of the poloidal magnetic flux profile $\psi(\rho,t)$ and a user-specified combination of the kinetic profiles $T_{e,i}(\rho,t)$ and $n_{e,i}(\rho,t)$. The MHD equilibrium and the kinetic profiles not solved for, are provided as inputs (and are allowed to vary in time). Note that the MHD equilibrium impacts the PDEs through coefficients depending on the geometry of the flux surfaces, i.e. $V'_\rho = \frac{\partial V}{\partial \rho}$, $g_0 = \langle \nabla V \rangle$, $g_1 = \langle |\nabla V|^2 \rangle$, $g_2 = \langle |\nabla V|^2 / R^2 \rangle$, $g_3 = \langle 1/R^2 \rangle$, where $\langle \cdot \rangle$ denotes flux surface averaging and V_ρ is the enclosed plasma volume, and through the poloidal current function $F = RB_\phi$. Time evolution of the external magnetic field or movements of the plasma can be taken into account through the term including the time derivative of the enclosed toroidal flux Φ_b. The equations for the simultaneous evolution of $\psi(\rho,t)$, $T_{e,i}(\rho,t)$ and $n_{e,i}(\rho,t)$ are (as indicated, the time derivatives are evaluated at constant ρ) [14]:

$$\sigma_\parallel \left(\left.\frac{\partial \psi}{\partial t}\right|_\rho - \frac{\rho \dot{\Phi}_b}{2\Phi_b} \frac{\partial \psi}{\partial \rho} \right) = \frac{F^2}{16\pi^2 \mu_0 \Phi_b^2 \rho} \frac{\partial}{\partial \rho} \left[\frac{g_2 g_3}{\rho} \frac{\partial \psi}{\partial \rho} \right] - \frac{B_0}{2\Phi_b \rho} V'_\rho [j_{bs} + j_{aux}] \quad (1)$$

$$\frac{3}{2} \frac{1}{(V'_\rho)^{5/3}} \left(\left.\frac{\partial}{\partial t}\right|_\rho - \frac{\dot{\Phi}_b}{2\Phi_b} \frac{\partial}{\partial \rho} \rho \right) [(V'_\rho)^{5/3} n_{e,i} T_{e,i}] = \frac{1}{V'_\rho} \frac{\partial}{\partial \rho} \left[\frac{g_1}{V'_\rho} n_{e,i} \chi_{e,i} \frac{\partial T_{e,i}}{\partial \rho} - \frac{5}{2} T_{e,i} \Gamma_{e,i} g_0 \right] + P_{e,i} \quad (2)$$

$$\frac{1}{V'_\rho} \left(\left.\frac{\partial}{\partial t}\right|_\rho - \frac{\dot{\Phi}_b}{2\Phi_b} \right) [V'_\rho n_{e,i}] = -\frac{1}{V'_\rho} \frac{\partial \Gamma_{e,i}}{\partial \rho} + S_{e,i} \quad (3)$$

with particle flux $\Gamma_{e,i} = -\frac{g_1}{V'_\rho} D_{e,i} \frac{\partial n_{e,i}}{\partial \rho} + g_0 V_{e,i} n_{e,i}$.

Equation (1) describes the diffusion of the poloidal magnetic field (or equivalently the parallel

current density) due to finite plasma resistivity, whilst (2) and (3) describe respectively the transport of thermal energy and particles (for ions and electrons), dominated by turbulent fluxes driven by plasma micro-instabilities. In practice, (2) is developed to a state evolution equation for $T_{e,i}(\rho,t)$, with $n_{e,i}$ either solved for with (3) or user-specified. In typical RAPTOR simulations, (3) is solved for the electron species, while ion and impurity densities are constrained by the equations imposing plasma quasi-neutrality ($n_e = \sum_j Z_j n_j$) and the plasma effective charge ($n_e Z_{eff} = \sum_j Z_j^2 n_j$), with either the main impurity density or the effective charge number pre-defined.

Heating, current drive and fueling sources are either internally calculated or prescribed. The bootstrap current density $j_{bs} = \langle \mathbf{j_{bs}} \cdot \mathbf{B} \rangle$ is self-consistently calculated with the Sauter formula [31], [32]. Heating sources and sinks due to ohmic power, bremsstrahlung, line radiation and electron-ion equipartitioning are internally evaluated as well. The radial deposition profile of electron cyclotron heating is either written as a sum of gaussians with different locations and widths or as a sum of spline basis functions, as illustrated in Section 3. The ad-hoc formula presented in [4] is used to capture the trend of reducing current drive efficiency for increasing deposition radius. Note that this feature is important for the optimization problems maximizing confinement by tailoring the current density described in later sections of this paper. The tuning of a scalar factor multiplying this expression allows to match the predictions to the results of experiments or more advanced simulations. The neutral beam profiles used in Section 4 are obtained from the PENCIL model [33] in the JETTO transport code [34].

The above set of equations features multiple couplings and non-linearities. By requiring analytical gradients for the dependencies of the coefficients on the plasma state, efficient implicit time stepping and non-linear optimization schemes are enabled. As we shall see, the new stationary state solver also takes full advantage of these analytical Jacobians.

In (2) and (3), analytical formulae are required to evaluate the local thermal diffusivities $\chi_{e,i}(\rho,t)$, particle diffusion coefficients $D_{e,i}(\rho,t)$ and pinch terms $V_{e,i}(\rho,t)$. While the ITER optimization results of Section 4 use the full QLKNN transport model, the illustrative examples shown in Sections 2 and 3 apply a simple ad-hoc formula for χ_e [4], taking into account the experimental observations of enhanced energy confinement for higher plasma current and for negative magnetic shear s. As this ad-hoc transport model plays a central role in the optimization problem discussed in Section 3, the analytic formula is repeated here:

$$\chi_e = \chi_{neo} + c_{ano}\rho q F(s) + \chi_{central} e^{-\rho^2/\delta_0^2} \tag{4}$$

with

$$F(s) = a_{ic}/[1 + e^{w_{ic}(d_{ic}-s)}] + (1 - a_{ic}) \tag{5}$$

The factor $F(s)$ multiplying the anomalous transport term provides improved electron energy confinement for negative magnetic shear, consistent with TCV experimental findings [35], [36]. The value of c_{ano} controls the global level of anomalous diffusion and is usually set empirically, to match the experimentally observed confinement time for a given level of plasma heating.

In Section 4, the QuaLiKiz neural networks presented in [15] evaluate the transport coefficients and the Jacobians containing the derivatives of the network outputs with respect to the 10 inputs. These Jacobians allow for the fully analytical evaluation of the derivatives of the transport coefficients to the plasma state through the meticulous application of the chain rule in the RAPTOR-QLKNN interface.

The boundary conditions accompanying these equations are $\frac{\partial \psi}{\partial \rho}|_{\rho=0} = 0$, $\frac{\partial T_{e,i}}{\partial \rho}|_{\rho=0} = 0$, $\frac{\partial n_{e,i}}{\partial \rho}|_{\rho=0} = 0$ (since $\rho = 0$ corresponds to the magnetic axis), $T_{e,i}(\rho = 1,t) = T_{e,i\ b}(t)$,

$n_{e,i}(\rho = 1,t) = n_{e,i\ b}(t)$ (the temperature and density boundary conditions can also be imposed at the pedestal top $\rho = \rho_{ped}$ to simulate H-modes) and $\frac{g_2 g_3}{\rho}\frac{\partial \psi}{\partial \rho}|_{\rho=1} = \frac{16\pi^3 \mu_0 \Phi_b}{F}|_{\rho=1} I_p(t)$.

2.2. Numerical implementation

Substituting the radial profiles constituting the plasma state by the sum of a set of finite element basis functions, the infinite-dimensional PDEs are discretized in space. Projecting the resulting equations on the set of basis functions and subsequently applying integration by parts, finite-dimensional ODEs in the finite element coefficients $\hat{\psi}$, $\hat{\mathbf{T}}_{\mathbf{e,i}}$ and $\hat{\mathbf{n}}_{\mathbf{e,i}}$ emerge:

$$\mathbf{F} = \mathbf{0} = -\mathbf{M}_\psi \dot{\hat{\psi}} - \mathbf{D}_\psi \hat{\psi} + \mathbf{B}_\psi \mathbf{u} + \mathbf{f}_\psi \tag{6}$$

$$\mathbf{G} = \mathbf{0} = -\mathbf{M}_{\mathbf{T_{e,i}}} \dot{\hat{\mathbf{T}}}_{\mathbf{e,i}} - \mathbf{D}_{\mathbf{T_{e,i}}} \hat{\mathbf{T}}_{\mathbf{e,i}} + \mathbf{B}_{\mathbf{T_{e,i}}} \mathbf{u} + \mathbf{f}_{\mathbf{T_{e,i}}} \tag{7}$$

$$\mathbf{H} = \mathbf{0} = -\mathbf{M}_{\mathbf{n_{e,i}}} \dot{\hat{\mathbf{n}}}_{\mathbf{e,i}} - \mathbf{D}_{\mathbf{n_{e,i}}} \hat{\mathbf{n}}_{\mathbf{e,i}} + \mathbf{B}_{\mathbf{n_{e,i}}} \mathbf{u} + \mathbf{f}_{\mathbf{n_{e,i}}} \tag{8}$$

The equations (6), (7) and (8) are derived from the respective equations (1), (2) and (3). The matrices **M**, **D** and **B** and the vectors **f** follow from the finite element discretization procedure. The *Actuator vector* **u** contains all external actuator inputs (including the total plasma current I_p, e.g. $\mathbf{u} = [I_p, P_{ec}, P_{nb}]^T$). Compacting the notation by introducing *state vector* $\mathbf{x} = [\hat{\psi}^T, \hat{\mathbf{T}}_{\mathbf{e,i}}^T, \hat{\mathbf{n}}_{\mathbf{e,i}}^T]^T$ and residue function $\mathbf{f} = [\mathbf{F}^T, \mathbf{G}^T, \mathbf{H}^T]^T$, a state evolution equation is obtained:

$$\mathbf{f}(\dot{\mathbf{x}}(t), \mathbf{x}(t), \mathbf{u}(t)) = 0 \tag{9}$$

Applying time-constant actuator inputs **u** and excluding transient phenomena (e.g. due to MHD activity), the plasma state $\mathbf{x}(t)$ evolves to a stationary solution $\mathbf{x_{SS}}$, characterized by time-independent profiles for the current density and the kinetic quantities. Whenever one is solely interested in the final state reached by the plasma (e.g. when optimizing the flat-top phase of a tokamak plasma discharge), it makes sense to solve directly for the stationary plasma profiles, neglecting the dynamics which are computationally costly to simulate. In equation (1), the radial derivative $\frac{\partial \psi(\rho,t)}{\partial \rho}$ is proportional to the current enclosed by the magnetic flux surface labeled by ρ, while the temporal derivative $\frac{\partial \psi(\rho,t)}{\partial t}$ equals the local loop voltage U_{pl}, the driving force for inductive current. A state can hence be considered stationary if the kinetic profiles are time-constant and the loop voltage is radially flat:

$$\frac{\partial}{\partial t} T_{e,i} = 0,\ \frac{\partial}{\partial t} n_{e,i} = 0 \text{ and } \frac{\partial}{\partial \rho}\left[\frac{\partial}{\partial t}\psi\right] = \frac{\partial}{\partial \rho} U_{pl} = 0 \tag{10}$$

Note that for a steady state $\frac{\partial \psi(\rho,t)}{\partial t} = U_{pl} = 0$, which is more restrictive: in a steady state, no inductive current is driven, meaning the plasma current is fully sustained by bootstrap current and auxiliary current.

The conditions imposed by equations (10) constrain the time derivative of the state vector $\dot{\mathbf{x}}_{\mathbf{SS}}$ to the following expression:

$$\dot{\mathbf{x}}_{\mathbf{SS}} = \left[\dot{\hat{\psi}}_{\mathbf{SS}}{}^T, \dot{\hat{\mathbf{T}}}_{\mathbf{e,i\ SS}}{}^T, \dot{\hat{\mathbf{n}}}_{\mathbf{e,i\ SS}}{}^T\right]^T, \text{ with} \tag{11}$$

$\dot{\hat{\psi}}_{\mathbf{SS}}{}^T = U_{pl}[1,1,...,1]^T$, $\dot{\hat{\mathbf{T}}}_{\mathbf{e,i\ SS}}{}^T = [0,0,...,0]^T$, $\dot{\hat{\mathbf{n}}}_{\mathbf{e,i\ SS}}{}^T = [0,0,...,0]^T$.

In other words: for a stationary plasma, the state vector time derivative is described by a single scalar, i.e. the value of the constant loop voltage U_{pl}.

Finding the stationary solution hence amounts to solving the non-linear set of equations:

$$\mathbf{f}(\dot{\mathbf{x}}_{\mathbf{SS}}(U_{pl}), \mathbf{x}_{\mathbf{SS}}, \mathbf{u}_{\mathbf{SS}}) = 0 \tag{12}$$

Since the number of equations equals the number of finite element coefficients n_{FE}, the non-linear system can be solved for n_{FE} unknown variables. The solution profile of the poloidal magnetic flux can be increased with a constant value without changing the physical interpretation. As a consequence of this gauge freedom, $n_{FE}-1$ independent variables describe the fully unknown stationary state $\mathbf{x_{SS}}$. The final unknown variable in equation (12) can be chosen to be either the unknown loop voltage U_{pl} or any actuator command U_{SS} in $\mathbf{u_{SS}}$. This leads to two alternative formulations of the non-linear root-finding problem:

- *option 1*: find the loop voltage resulting in a stationary state for given actuator commands $\mathbf{u_{SS}}$
- *option 2*: find the actuator command resulting in a stationary state for given loop voltage U_{pl}

As both cases have interesting use-cases, both options are implemented in the stationary state solver.

The system of non-linear equations is solved iteratively with a Newton-Raphson method. A vector $\mathbf{z} \in \mathbb{R}^{n_{FE}}$ is defined, containing all unknown variables, i.e. $\mathbf{z}^T = [\mathbf{x_{SS}}^T, U_{pl}]^T$ (*option 1*) or $\mathbf{z}^T = [\mathbf{x_{SS}}^T, U_{SS}]^T$ (*option 2*). Solving for the stationary state hence amounts to solving the non-linear system of equations $\mathbf{f}$ for the unknown set of variables $\mathbf{z}$. The state function $\mathbf{f}$ is evaluated for an initial guess $\mathbf{z_0}$, along with the Jacobian $\partial\mathbf{f}/\partial\mathbf{z}$. The Jacobian can be evaluated analytically by careful application of the chain rule to obtain $\partial\mathbf{f}/\partial\dot{\mathbf{x}}$, $\partial\mathbf{f}/\partial\mathbf{x}$ and $\partial\mathbf{f}/\partial\mathbf{u}$ and by passing the parametrizations $\partial\dot{\mathbf{x}}/\partial\mathbf{z}$, $\partial\mathbf{x}/\partial\mathbf{z}$ and $\partial\mathbf{u}/\partial\mathbf{z}$ inside the solver. A parameter vector update $\mathbf{z_{i+1}} = \mathbf{z_i} + \Delta\mathbf{z}$ is calculated by solving the locally linearized equation $\mathbf{f} = -\frac{\partial\mathbf{f}}{\partial\mathbf{z}}\Delta\mathbf{z}$ for the increment $\Delta\mathbf{z}$. To make the solution procedure more robust, the step size $|\Delta\mathbf{z}|$ is reduced whenever the update causes the plasma profiles to exhibit unphysical behaviour‡ or the residual error increases (i.e. $|\mathbf{f_{i+1}}| > |\mathbf{f_i}|$). This algorithm is repeated iteratively until the norm of the evaluated equations is smaller than a pre-defined value.

To illustrate the gain in computation time that can be obtained by directly solving for the stationary plasma state (and the plasma loop voltage, applying *option 1* of the solver), the time evolution of radial profiles in a time dependent RAPTOR run is compared to the stationary solution. The state consists of the T_e profile and the ψ profile. A standard MHD equilibrium for the TCV tokamak is selected, with a plasma current $I_p = 200\,\mathrm{kA}$, an imposed electron density profile with $n_{e0} = 10^{19}\,\mathrm{m}^{-3}$ and electron cyclotron heating ($P_{aux} = 1\,\mathrm{MW}$) with a gaussian auxiliary power deposition profile centered around $\rho = 0.4$, providing co-current drive. Figure 1 presents time traces of the distance of the plasma profiles (ψ and T_e solved for 1 s) to the stationary solution. The plasma state clearly evolves to the stationary solution at the slow timescale of current diffusion (note the time constant $\tau = 170\,\mathrm{ms}$ of the superimposed exponentials on Figure 1). Due to the non-linear coupling of equations (2) and (1), the temperature profile also evolves on this slow timescale. Assuming a current redistribution time of about $\tau_{crt} = 170\,\mathrm{ms}$ and a typical RAPTOR time step (for TCV plasmas) of 5 ms, more than 100 time steps would be needed to simulate up until $t = 3\tau_{crt}$, where a relaxed state can safely be assumed, each time step requiring the solution of a non-linear system of equations. The stationary state solver on the other hand requires only 5 Newton steps to determine the stationary state of both profiles with a residue $r_i = |\mathbf{f_i}|$ below 10^{-10} (more details on the convergence rate are presented in Appendix A).

Let us present a simple example on how the stationary state solver can be applied to obtain the stationary plasma profiles $\psi(\rho)$ and $T_e(\rho)$, as well as the level of electron cyclotron heating

‡ Updated profiles are considered unphysical if any of the following quantities becomes (locally) negative: $T_{e,i}$, $n_{e,i}$ or $\frac{\partial\psi}{\partial\rho}$.

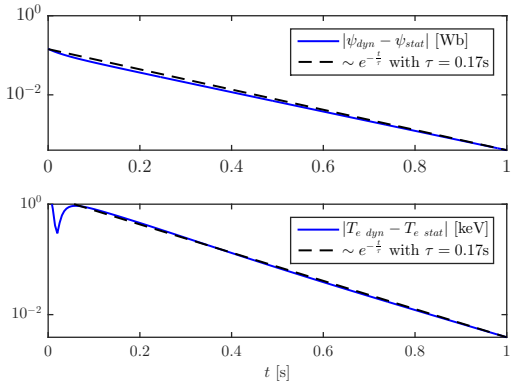

Figure 1. Time evolution to stationary state Time traces of the distance (2-norm of the vector containing the difference on 20 radial grid points) of the ψ and T_e profiles in a time dependent RAPTOR simulation (*dyn*) to their respective stationary solutions (*stat*) for a TCV plasma (1 s simulation with time step 5 ms). The time constant $\tau = 170$ ms of the superimposed exponentials show that both T_e and ψ evolve to a relaxed shape at the slow timescale of current diffusion.

and current drive required to sustain a stationary plasma on the TCV tokamak at a user-defined level of the loop voltage. Assumptions regarding MHD equilibrium, total plasma current, electron cyclotron heating and current drive deposition and electron density are identical to the previous example. The magnitude of the electron cyclotron power P_{aux} is now considered an unknown, while the requested loop voltage is directly introduced in the non-linear equation (12), which is hence solved to get the plasma state $\mathbf{x_{SS}}$ together with the actuator request $\mathbf{u_{SS}}$ (illustrating *option 2* of the non-linear solver).
Two cases are considered, respectively imposing loop voltages of $U_{pl} = 0.5$ V (left hand side of Figure 2) and $U_{pl} = 0$ V (right hand side of Figure 2). While the first case allows for a large fraction of ohmic current driven by the tokamak central solenoid, the second case explores steady state operation with no inductive current. Although actual plasma profile predictions depend on the tuning of parameters in the ad-hoc transport model, this simulation illustrates how the stationary state solver can be used to find the actuator command resulting in a stationary state with an imposed loop voltage U_{pl}. An increased auxiliary power is required ($P_{aux} = 1.9$ MW for $U_{pl} = 0$ V compared to $P_{aux} = 0.6$ MW for $U_{pl} = 0.5$ V) to sustain the entire plasma current with the externally driven electron cyclotron current and the internally generated bootstrap current. The non-linear problem of retrieving consistent stationary temperature and current density profiles, including the effects of T_e-dependent current drive efficiency and $\frac{\partial T_e}{\partial \rho}$-dependent bootstrap current, is successfully solved. Note that steady state TCV tokamak plasmas with plasma currents up to $I_p = 210$ kA have been sustained with the available electron cyclotron heating capacity [37], [38], [39].

3. Non-linear model-based optimization of stationary tokamak plasma profiles

In this section we show how the stationary state solver is implemented in a non-linear optimization routine. The aim is to find the combination of actuator commands (parametrized by a vector with optimization variables $\mathbf{p}$) maximizing a measure of performance of the plasma state, while conforming to imposed bounds on the plasma state and technical

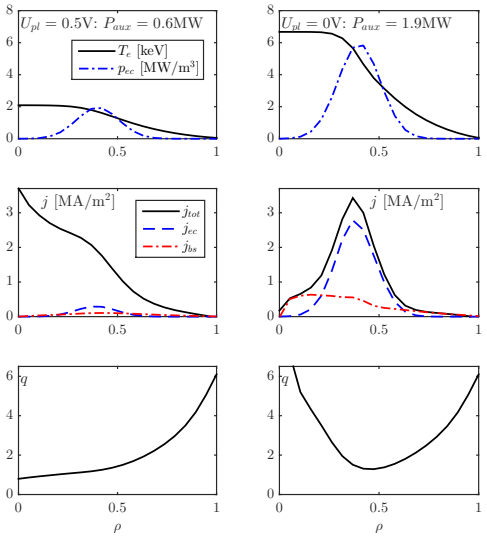

Figure 2. Illustration stationary state solver Illustrative TCV simulation of stationary state profiles for $U_{pl} = 0.5V$ (left) and $U_{pl} = 0V$ (right). As expected, an increased auxiliary power is required ($P_{aux} = 1.9$MW for $U_{pl} = 0$V compared to $P_{aux} = 0.6$MW for $U_{pl} = 0.5$V) to sustain the entire plasma current with the externally driven electron cyclotron current and the internally generated bootstrap current.

constraints of the tokamak. The performance of the plasma is captured in a cost function J. Examples of optimization goals include minimum auxiliary power P_{aux} and maximum stored thermal energy W_{th}, nuclear fusion power P_{fus} or bootstrap current I_{bs}. A weighted sum allows for the construction of a composite cost function. Non-linear constraints on the plasma state can for example inhibit the formation of a $q = 1$ surface, or avoid known disruptive limits. Simple linear constraints for the optimization variables can be used to impose limits on actuator commands, e.g. limiting the available auxiliary power. The vector of optimization variables can contain lumped variables (e.g. total plasma current, total auxiliary power), as well as a number of coefficients defining a radially distributed profile through a set of basis functions (e.g. the radial distribution of auxiliary heating on a set of basis functions).

Appendix B presents the mathematical formulation of a generic parameter optimization problem for the stationary plasma state, as well as a solution procedure based on non-linear programming. The described routine can be applied to optimize stationary plasma profiles, by tailoring the radial distribution of auxiliary heating $p_{aux}(\rho)$ and externally driven current density $j_{aux}(\rho)$. For the present illustrative example, the stationary state solver in the inner iteration loop assumes a standard TCV MHD equilibrium and a plasma current $I_p = 200$kA, and solves for the loop voltage in addition to the T_e and ψ profiles (*option 1* of the solver). The total electron cyclotron power is constrained to $P_{aux} = 3$MW, which is assumed to sustain an H-mode. A linear temperature pedestal is imposed in the region $\rho = [\rho_{ped} = 0.9, 1]$, with the temperature pedestal as a boundary condition for the core T_e profile solved by RAPTOR. The imposed n_e profile is consistent with H-mode operation, with $n_{e0} = 10^{19}\,\mathrm{m}^{-3}$.

The goal of the parameter optimization problem presented here is to maximize the thermal

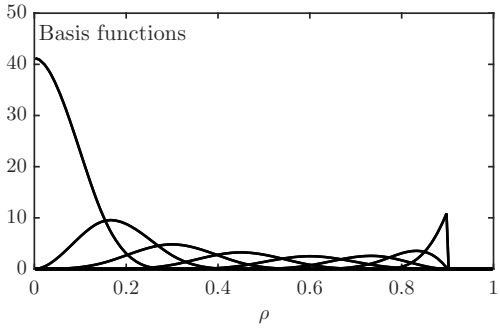

Figure 3. Spline basis functions This is the set of basis functions (cubic splines on $\rho = [0, \rho_{ped}]$ with $\rho_{ped} = 0.9$) for the construction of the radial distribution of auxiliary heating and current drive density. The basis functions are normalized to ensure for each basis function the correspondence of $p_i = 1$ to an integrated auxiliary heating contribution of 1 MW.

energy stored by the electrons, which can be formulated as the minimization of:

$$J = -W_{th} = -\frac{3}{2}\int_V n_e T_e dV \tag{13}$$

The radial auxiliary power profile is written as a linear combination of the basis functions $g_i(\rho)$ with $i \in [1, 2, ..., n_g]$, drawn in Figure 3 for $n_g = 8$§. The power deposited at different radial locations is parametrized by the values in the optimization vector $\mathbf{p}$ (the basis functions are normalized such that $p_i = 1$ corresponds to an integrated auxiliary heating contribution of 1 MW). For each basis function $g_i(\rho)$, both a contribution with positive and negative current drive efficiency are allowed, respectively encoded in p_i and p_{n_g+i} (pure heating can be obtained by assigning $p_i = p_{n_g+i}$). To summarize, the radial distribution profile of auxiliary heating and current drive is obtained by multiplying the basis functions with the corresponding power amplitudes in $\mathbf{p}$ (including a current drive efficiency η for j_{aux}):

$$p_{aux}(\rho) = \sum_{i=1}^{n_g} g_i(\rho)\left[p_i + p_{n_g+i}\right] \tag{14}$$

$$j_{aux}(\rho) = \sum_{i=1}^{n_g} g_i(\rho)\eta\left[p_i - p_{n_g+i}\right] \tag{15}$$

The total available power imposes a linear inequality constraint of type (B.1b) on the optimization variables:

$$\sum_{i=1}^{2n_g} p_i \leq P_{aux} \tag{16}$$

A non-linear inequality constraint of type (B.1c) on the state allows the algorithm to avoid solutions for which the q profile drops below $q = 1$. This constraint allows to avoid sawtooth activity, e.g. to avoid seeding deleterious NTMs [40].

$$\mathscr{C}_{q>1} = \left[\int_0^{\rho_e} \max\left(0, \frac{1}{q(\rho)} - 1\right) d\rho\right]^2 - \varepsilon \leq 0 \tag{17}$$

The obtained optimal plasma state is presented in Figure 4. The result is interesting as it

§ The choice of the number of basis functions results from a trade-off: although more basis functions allows the optimizer to find more optimal solutions (since the solutions accessible on a coarser basis are still achievable, in addition to radial distributions with more refined features), the risk for finding local minima increases. Furthermore, overfitted optima can be obtained, which generalize poorly when applied for slightly perturbed model parameters.

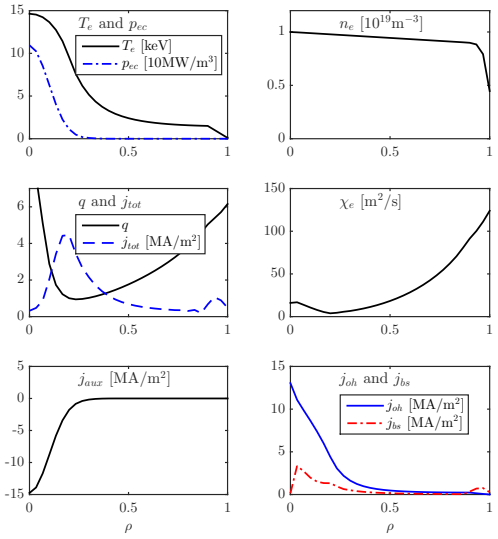

Figure 4. Illustration stationary state optimizer Radial distribution of electron cyclotron heating and current drive that maximize the stored electron thermal energy for a TCV plasma with fixed total auxiliary power $P_{aux} = 3\,\mathrm{MW}$. The optimizer finds that central counter-ECCD is the optimal choice to maximize T_e, yielding a total current density profile with an off-axis peak, creating an internal transport barrier in the T_e profile.

demonstrates the ability of the proposed optimization method to exploit non-trivial features of the transport model: driving negative current on-axis, the magnetic shear reaches a large negative value (due to the off-axis peak of the current density), which, through the ad-hoc transport model used [4], triggers a local drop in the electron heat diffusivity $\chi_e(\rho)$. The total plasma current $I_p = 200\,\mathrm{kA}$ is obtained by driving positive ohmic current (the stationary state solver finds the loop voltage U_{pl} necessary to drive the required ohmic current). The local drop in electron heat diffusivity χ_e results in a steep gradient for the T_e profile, known as an electron internal transport barrier. Note how the bootstrap current driven by both internal and edge transport barriers contributes to the off-axis current.

4. Optimization of the ITER hybrid scenario with RAPTOR coupled to QLKNN

Within the ITER scientific mission [41], the ITER hybrid scenario provides a potential road to long-pulse discharges ($t_{burn} > 1000\,\mathrm{s}$) with a high fusion gain $Q > 5$, providing a compromise between

- the *inductive reference scenario*, pursuing a fusion gain $Q > 10$ for a limited duration $t_{burn} \sim 400\,\mathrm{s}$ by operating at a high total plasma current ($I_p = 15\,\mathrm{MA}$), and
- the *steady state scenario*, achieving an extended discharge duration ($t_{burn} = 3000\,\mathrm{s}$, limited by cooling system limits) by operating at a lower total plasma current ($I_p \sim 9\,\mathrm{MA}$), driven entirely by non-inductive means (auxiliary current and bootstrap current).

The reduction of the total plasma current I_p requires operation at lower density (Greenwald density limit $n_{e\,Gw} = I_p/(\pi a^2)$ [42]) and negatively affects the energy confinement time

(IPB98(y,2) scaling law for ELMy H-mode plasmas [22] predicts $\tau_E \sim I_p^{0.93} n_e^{0.41}$) ‖. The success of hybrid and steady state scenarios hence rely on enhanced energy confinement, leading to an increase of both the nuclear fusion power and the internally driven bootstrap current. Contrary to some of the scenarios proposed for steady state operation, hybrid scenarios do not rely on the formation of internal transport barriers in the core plasma [44]. Lowering turbulent transport should be achieved through tailoring of the safety factor profile q, controlling the auxiliary current density deposition profile. The hybrid scenario envisions a q profile with a wide flat region in the center with $q > 1$ everywhere, avoiding the onset of sawtooth crashes. The absence of sawtooth triggered neoclassical tearing modes (NTMs) allows operation at increased values of β_N (assuming the resistive β limit to avoid the onset of (2,1)-NTMs is below the ideal limit $\beta_{N,max} = 4l_i$). Note that allocation of electron cyclotron current drive to avoid the onset of NTMs [45] is not taken into account in the present work.
The relatively large amount of localized ECCD on ITER allows for a high degree of q profile shaping. The shape of the q profile impacts micro-instabilities driving turbulent transport, as reported from both experiments and modelling for AUG and JET hybrid discharges [46], [47]. As discussed in [24] and [48], hybrid scenario plasmas are characterized by an increased value of s/q at the outer plasma radii, where s is the magnetic shear, which increases the ion temperature inverse scale length threshold for the onset of ITG-driven heat transport, the main turbulent heat transport channel for this scenario (non-zero ITG heat transport for $R/L_{T_i} > R/L^{ITG}_{T_i\ crit}$, where $L_{T_i} = aT_i/|\frac{\partial T_i}{\partial \rho}|$ with a the plasma minor radius). Alternative mechanisms, not descibed by the transport model applied in this paper, have been proposed to explain the improved confinement of hybrid scenarios, including the electromagnetic stabilisation of ITG turbulence, enhanced by both low magnetic shear and fast ions (which are more prevalent at lower density) and increased ExB shear turbulence stabilisation at lower density [49], [50].
The subsequent sections extensively apply the non-linear optimization routine described in Appendix B and make use of *option 1* of the novel stationary state solver described in Section 2, treating the plasma loop voltage as an unknown in addition to the requested plasma profiles, while prescribing the auxiliary power sources and plasma current I_p. Since the individual optimization problems are solved within minutes on standard hardware, the presented framework provides a versatile tool to explore various operational conditions and perform sensitivity analyses.

4.1. Modeling assumptions

Table 1 and Figure 5 present some stationary state quantities and profiles of the RAPTOR-QLKNN simulated plasma scenario referred to henceforth as the ITER hybrid reference case. This scenario is obtained by maximizing the fusion gain Q for a fixed total plasma current $I_p = 10.5\,\mathrm{MA}$, by varying the deposition location of the electron cyclotron heating and current drive (modeled as a gaussian curve with width $\Delta\rho = 0.15$), while constraining $q > 1$.

4.1.1. Stationary diffusion equations and boundary conditions For the ITER results presented in this paper, RAPTOR solves for transport of ion and electron heat and poloidal flux (i.e. T_e, T_i and ψ stationary diffusion equations). The reference temperature boundary conditions $T_{e\ ped} = 4.5\,\mathrm{keV}$ and $T_{i\ ped} = 4.5\,\mathrm{keV}$ are set at the pedestal location $\rho_{ped} = 0.9$.

‖ A recently published revised energy confinement scaling law ITPA20-IL [43], based on an ITER-like subset of the ITPA global H-mode confinement database (extended with new data from JET with the ITER-like wall and ASDEX Upgrade with the full tungsten wall), predicts a reduced density dependence, while maintaining a strong plasma current dependence: $\tau_E \sim I_p^{1.29} n_e^{0.15}$.

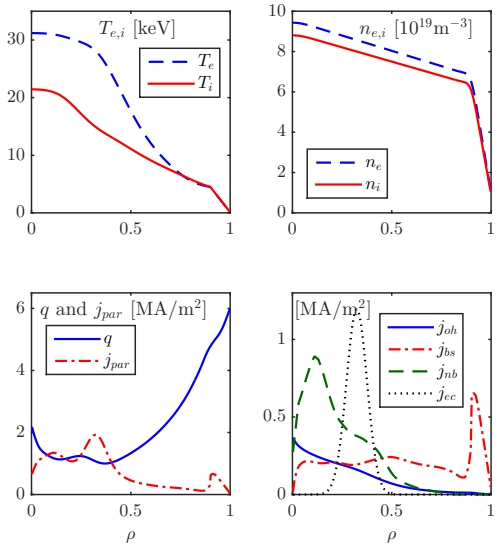

Figure 5. ITER hybrid reference case scenario Summary of radial profiles of the RAPTOR-QLKNN stationary state simulation referred to henceforth as the ITER hybrid reference case scenario ($I_p = 10.5\,\mathrm{MA}$).

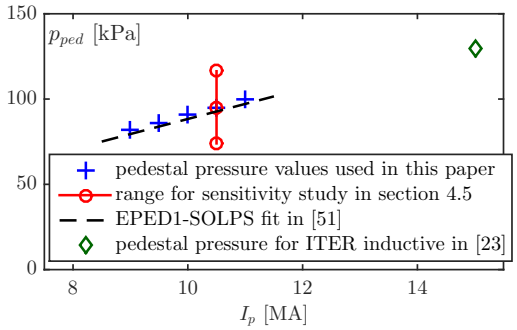

Figure 6. Overview pedestal pressures The pedestal pressures imposed within the simulations presented in this paper are compared to the EPED1-based scaling law for ITER moderate pedestal densities with SOLPS-compatible separatrix densities introduced in [51]. The increased and decreased pedestal pressures applied in the sensitivity study in Section 4.5 are also shown, in addition to the upper pressure 130 kPa for the ITER inductive scenario as reported in [23].

For $\rho > \rho_{ped}$, a linear temperature pedestal is imposed. The Neumann boundary condition for the ψ diffusion equation depends on the total plasma current I_p. A range of different total plasma currents is reviewed, considering $I_p = 10.5\,\mathrm{MA}$ as the reference case.

Although the addition of particle transport to the set of solved equations is straightforward, fixed density profiles are imposed for the stationary states modeled in this paper, with the exception of Section 4.6, where the RAPTOR-QLKNN density prediction is presented as part of a density profile sensitivity study. Imposing a density profile has the advantage of maintaining direct control over the Greenwald fraction $f_{Gw} = \langle n_e \rangle_{line} / n_{Gw}$ and the peaking

I_p	10.5 MA
B_0	5.3 T
a	2.0 m
R_0	6.2 m
I_{bs}/I_p	0.43
I_{ni}/I_p	0.89
P_{fus}	367 MW
P_{nb}	33 MW
P_{ec}	40 MW
$P_{rad\ tot} = P_{brem} + P_{line}$	22 MW
P_{sep}	124 MW
P_{LH}	77 MW
$W_{th\ tot}$	309 MJ
T_{i0}, $T_{i\ ped}$	21 keV, 4.5 keV
T_{e0}, $T_{e\ ped}$	31 keV, 4.5 keV
q_{95}	5.1
$\langle n_e \rangle_{line}/n_{e\ Gw}$	7.8×10^{19} m^{-3}/8.5×10^{19} m^{-3}=0.9
$n_{e0}/n_{e\ ped}$	9.4×10^{19} m^{-3}/6.8×10^{19} m^{-3}=1.4
$H_{y2,98}$	1.3
β_N	2.4
l_i	0.84
U_{pl}	3.7 mV
Q	5.0

Table 1. ITER hybrid reference case scenario Summary of physical quantities of the RAPTOR-QLKNN stationary state simulation referred to henceforth as the ITER hybrid reference case scenario.

factor $n_{e,i0}/n_{e,i\ ped}$. The reference density profiles used in this section are constructed by merging two linear segments (respectively for core and pedestal, considering a peaking factor of $n_{e,i0}/n_{e,i\ ped} = 1.4$). The resulting profile is smoothed to avoid a discontinuity in the bootstrap current density, while the first derivative is set to zero at the magnetic axis $\frac{\partial n_e}{\partial \rho}|_{\rho=0} = 0$. The density peaking can be quantified by the ratio $n_{e,i0}/\langle n_{e,i} \rangle_{vol} = 1.3$, which is a conservative value compared to the prediction for the ITER inductive scenario in [52]. Since the hybrid scenario operates at lower collisionality, a further increase of density peaking can be anticipated [53], [54]. The value of the electron density at the pedestal $n_{e\ ped}$ ($\rho_{ped} = 0.9$) is increased for increasing value of the total plasma current I_p, ensuring a line-averaged electron density below the Greenwald density limit ($\langle n_e \rangle_{line}/n_{e\ Gw} = 0.9$). In practice, the density pedestal can be controlled with peripheral pellet fueling on ITER. Note that the use of the line-averaged density to evaluate the Greenwald density fraction is conservative as experimental evidence links the limit to phenomena near the plasma edge, suggesting the potential of plasmas with peaked density profiles to operate at higher densities [55]. Recent work relates the H-mode density limit to ballooning stability limits at the separatrix, finding $n_{e\ sep}/n_{e\ Gw} \sim 0.4 - 0.5$ as an upper limit [56]. This effectively provides an indirect upper limit for $n_{e\ ped}$ due to the stiffness of pedestal transport.

The ion density profile $n_i(\rho)$ (sum over Deuterium and Tritium species), is inferred from

the $n_e(\rho)$ profile by requiring quasi-neutrality and imposing $Z_{eff} = 1.6$, considering Neon ($Z = 10$) as the only impurity, aggregating the impact of He, Be, Ne, W etc.
Note that the linear increase of the density pedestal with plasma current I_p results (for constant $T_{e,i\ ped}$) in a linear scaling of the pedestal pressure, which is consistent with EPED1 simulations for ITER [51]. Figure 6 compares the pedestal pressures imposed within the simulations presented in this paper to the EPED1-based scaling law for ITER moderate pedestal densities with SOLPS-compatible separatrix densities introduced in [51]. The increased and decreased pedestal pressures applied in the sensitivity study in Section 4.5 are also shown, in addition to the upper pressure 130 kPa for the ITER inductive scenario as reported in [23]. Note that the calculation of consistent separatrix densities is out of the scope of this paper. The pedestal pressures applied in this paper are very close to the scaling law projections, giving confidence in the applied boundary conditions.

4.1.2. MHD equilibrium geometry A consistent MHD equilibrium for the $I_p = 10.5$ MA reference case is found by iterative application of the RAPTOR stationary state solver and the CHEASE fixed-boundary MHD equilibrium solver [57]. The shape of the last closed flux surface is reproduced from [58]. Within the optimization routine, the geometric terms in the transport equations, reflecting the underlying MHD equilibrium, are not updated. This approach is justified if the impact of these geometric factors on the obtained stationary radial profiles is moderate. This has been verified explicitly for the simulations shown in this paper by performing iterations between RAPTOR and CHEASE. Including more complex modeling of pedestal stability and turbulent transport, the effect of the equilibrium geometry could become more important and require self-consistent iterations of the MHD equilibrium.

4.1.3. Auxiliary heating and current drive Auxiliary heating and current drive are provided by electron cyclotron waves and neutral beam injection. The combination of these technologies was found to yield the best performance in the optimized ITER hybrid scenario described in [24]. The maximal heating powers are set to $P_{nb} = 33$ MW and $P_{ec} = 40$ MW, considering the availability of a 20 MW electron cyclotron upgrade in addition to the ITER baseline heating mix, as proposed in [23] for improved H-mode accessibility margin. Alpha and bremsstrahlung power are calculated by the respective RAPTOR source and sink modules [5].
The radial deposition profile of electron cyclotron heating and current drive results from an optimization procedure, as described in the subsequent section. The electron cyclotron current drive efficiency is modeled in RAPTOR with a T_e/n_e dependency, resulting in a strong efficiency drop when sweeping the deposition location away from the core. The efficiency factor is tuned to obtain a dimensionless current drive efficiency (as defined in [59]: $\zeta = \frac{e^3 n I_{ec} R}{\varepsilon_0^2 P_{ec} T}$) similar to the efficiency modelled in [24] by application of the analytic approximations developed in [60], i.e. $\zeta \sim 0.35$.
The JINTRAC integrated modeling suite with the JETTO transport solver [34] is used to evaluate consistent neutral beam profiles for the stationary states found at $I_p = 10$ MA and $I_p = 11$ MA with optimized electron cyclotron deposition (applying the QLKNN transport model like in the respective RAPTOR runs). The relaxed final state of time dependent JETTO simulations for $I_p = 10$ MA and $I_p = 11$ MA (with the respective density profiles imposed) converge to a stationary state, with consistent neutral beam profiles evaluated by the PENCIL module [33]. Radial profiles of neutral beam deposition for different density profiles are calculated in RAPTOR by interpolating linearly with respect to the density at the magnetic axis n_{e0}, e.g. $j_{nb}(\rho) = j_{nb\ 10\mathrm{MA}}(\rho) + \frac{n_{e0} - n_{e0\ 10\mathrm{MA}}}{n_{e0\ 11\mathrm{MA}} - n_{e0\ 10\mathrm{MA}}}(j_{nb\ 11\mathrm{MA}}(\rho) - j_{nb\ 10\mathrm{MA}}(\rho))$,

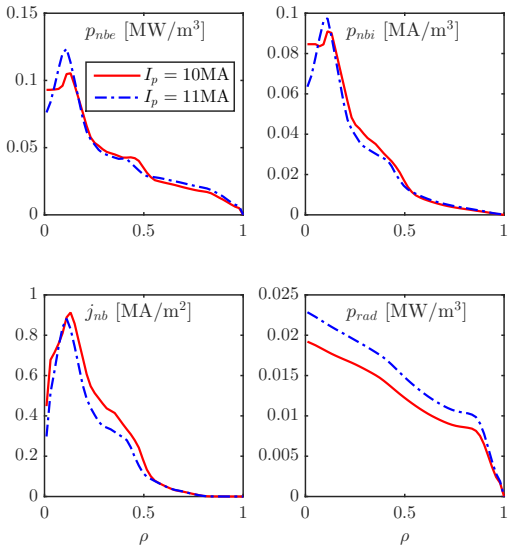

Figure 7. Overview JETTO NBI and line radiation profiles Neutral beam and line radiation profiles in the relaxed final state of time dependent JETTO-QLKNN simulations for $I_p = 10\,\mathrm{MA}$ and $I_p = 11\,\mathrm{MA}$ (with the respective density profiles profiles imposed). These profiles provide the inputs to the interpolation procedure to evaluate the corresponding source/sink terms in RAPTOR.

with $n_{e0\ 10\mathrm{MA}} = 8.9 \times 10^{19}\,\mathrm{m}^{-3}$ and $n_{e0\ 11\mathrm{MA}} = 9.8 \times 10^{19}\,\mathrm{m}^{-3}$. An identical interpolation procedure is applied to evaluate the radial line radiation profiles. Figure 7 shows the neutral beam and line radiation profiles obtained from the JETTO predictive runs at $I_p = 10\,\mathrm{MA}$ and $I_p = 11\,\mathrm{MA}$, which provide the inputs to the interpolation procedure in RAPTOR. The proposed linear interpolation based on n_{e0} can be justified by the main dependence of these profiles on the density, as well as by the relatively small variation of the respective profiles throughout the explored range of operating points, as apparent from Figure 7 (under the present assumption of a fixed density peaking factor). Further efforts for inclusion of (reduced) physics modules to evaluate neutral beam deposition profiles and line radiation profiles are however clearly desirable.

4.1.4. Transport flux predictions Heat diffusivities $\chi_{e,i}$ are modeled with QLKNN [15], a neural network emulation of the QuaLiKiz quasi-linear gyrokinetic transport model [16], [17]. The model predicts that the ion and electron temperature gradients in the hybrid scenario operating space are dominated by ITG instabilities, with subdominant TEM. Note that the TEM contribution could become more important when the ITG stabilisation by electromagnetic and fast ion effects are accounted for, which is outside the scope of the QuaLiKiz model. For the heat diffusivity predictions in this paper, only the dominant ITG turbulent transport channel is hence maintained and the other channels (ETG, TEM) are disabled within QLKNN. The inclusion of TEM turbulence may impact the density peaking [61], but the bulk of simulations carried out in this work are with heat transport only.
Hybrid scenarios are characterized by a high value of the normalized pressure gradient $\alpha = \frac{d\beta}{d\rho} q^2 R_0$ (where β is the ratio of the volume averaged kinetic pressure to the magnetic

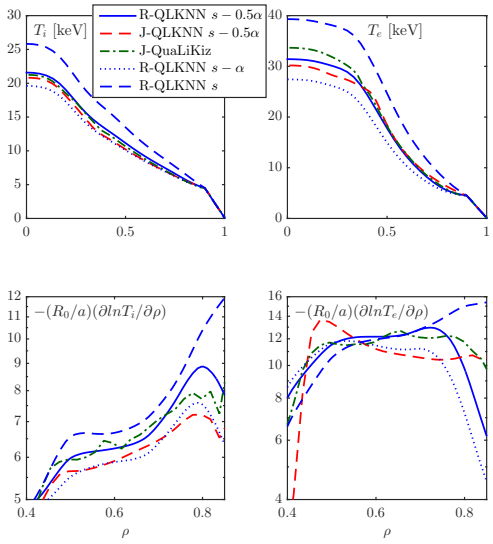

Figure 8. Transport model benchmark A comparison is shown of the temperature and temperature inverse scale length profiles obtained with RAPTOR-QLKNN (*R-QLKNN*) at the reference current $I_p = 10.5\,\mathrm{MA}$, feeding the neural network shear input with either s, $s-0.5\alpha$ or $s-\alpha$, to relaxed JETTO profiles (time dependent JETTO run, solving solely for electron and ion heat diffusion, ensuring a q profile identical to the RAPTOR run), applying respectively the $s-0.5\alpha$ corrected QLKNN transport model (*J-QLKNN*) and full QuaLiKiz (*J-QuaLiKiz*).

pressure) towards the edge of the plasma. The standard version of QLKNN does not take into account the impact of α on transport (α is not included in any of the neural network inputs). In the QuaLiKiz geometry model, the quantity α roughly modifies the shear $s \rightarrow s-\alpha$. Not taking into account this decrease of the effective shear leads to a systematic over-prediction of temperatures for the ITER hybrid scenario (consider the scaling for the ITG threshold mentioned earlier: $R/L_{T_{i\ crit}} \sim s/q$). Standalone studies with the full QuaLiKiz model show that within the ITER hybrid scenario parameter range, a decent proxy for the impact of α on predicted transport can be obtained by feeding the model an effective shear: $s_{eff} = s-0.5\alpha$. This ad-hoc rule motivates a transformation of the shear input of the neural network $s \rightarrow s-0.5\alpha$ when modeling hybrid scenarios, leading to excellent agreement of the temperature profiles predicted respectively by JETTO-QuaLiKiz and JETTO-QLKNN with adjusted neural network inputs.

The $s \rightarrow s-0.5\alpha$ transformation is hence applied for ITER hybrid modeling in RAPTOR-QLKNN. To illustrate the validity of this approach, Figure 8 compares the temperature and temperature inverse scale length profiles obtained with RAPTOR-QLKNN at the reference plasma current $I_p = 10.5\,\mathrm{MA}$, feeding the neural network shear input with either s, $s-0.5\alpha$ or $s-\alpha$, to relaxed JETTO profiles (time dependent JETTO run, solving solely for electron and ion heat diffusion, ensuring a q profile identical to the RAPTOR run), applying respectively the $s-0.5\alpha$ corrected QLKNN transport model and full QuaLiKiz. The full QuaLiKiz simulation is in close agreement with both JETTO and RAPTOR simulations applying the $s-0.5\alpha$ correction, as remaining differences can be accounted for to some extent by different smoothing of the predicted heat diffusivity profiles.

Although the transport model predicts low transport levels at low radii, flattened temperature

profiles toward the magnetic axis are anticipated, even in the absence of sawtooth activity. This statement is motivated by experimental measurements and the results described in [62], where the presence of kinetic ballooning modes in the hybrid plasma core is predicted. This is taken into account by adding a gaussian to the diffusivity predictions, centered at $\rho = 0$, with width $\Delta\rho = 0.1$ and height $\chi_{e,i\,0} = 2\,\mathrm{m}^2/\mathrm{s}$.

As noted above, electromagnetic and fast ion effects are missing in the applied transport model. These effects are seen to increase confinement in present-day hybrid scenarios [49], [63], while recent work indicates that ITG suppression by fast alphas will also allow improved confinement in ITER [50], [64]. Although the quantitative degree of confinement improvement for ITER due to these effects is uncertain, the levels of core confinement presented in this paper could hence be under-predicted, providing a conservative lower bound for ITER hybrid performance. Note however that the s/q optimization path is largely independent from these considerations, with the trends seen in ECCD deposition modification and impact of s/q on ITG thresholds holding regardless of the electromagnetic and fast ion effects.

The reference case simulation predicts a strong temperature difference between ions and electrons is maintained in stationary state ($T_{e0}/T_{i0} = 1.46$). In [65] the small impact of dominant electron heating on T_{e0}/T_{i0} was illustrated for the ITER inductive scenario. A reduced equipartition heating due to the lower density allows for a stronger temperature ratio in the hybrid scenario. While the stiffness of the ion temperature profile predicted by the present model results in a very weak dependence of the fusion power on the ion heating, the electron profile is notably less stiff, hence resulting in a strong dependence of plasma resistivity, bootstrap current and electron cyclotron current drive efficiency on the level of electron heating.

4.2. Optimization of the electron cyclotron deposition profile

The shape of the q profile can be tailored to some extent by optimizing the radial deposition profile of auxiliary current drive sources. The present study considers the optimization of the electron cyclotron current drive profile. Various approaches can be envisioned to parametrize the radially distributed deposition profile in terms of a set of optimization variables. Without making an a priori assumption on the shape of these profiles, the radial deposition profile can be written as the sum of a set of cubic spline basis functions. The procedure for optimizing a distributed quantity on a basis of splines, including the formulation of cost and constraint functions, is discussed in detail in Section 3 and Appendix B.

The optimization problem under consideration is solved on several spline bases, with an increasing number of splines, hence increasing the degrees of freedom available to fine-tune the radial electron cyclotron deposition profile. The behaviour of the resulting optima is presented in Figure 9. Increasing the number of splines above 7 has a minor impact on the resulting maximum fusion gain Q. This can be understood as follows: to obtain maximum energy confinement, hybrid scenarios maximize the outermost radius with safety factor close to unity, which then results in a maximum magnetic shear further outward. The increased ratio s/q raises the onset threshold for ITG-driven turbulence. The same logic was outlined in [24], where the electron cyclotron current drive distribution was manually tailored to have the q profile clamped to the $q = 1$ constraint at the outermost radius that can be achieved with the available electron cyclotron power. The execution of this procedure is now fully automated. Figure 9 shows that with spline bases containing respectively 7 and 9 basis functions, the q profile can be clamped to $q = 1$ at a strikingly similar outermost radius. The outer s and q profiles are virtually identical, yielding similar ITG threshold enhancements and hence fusion

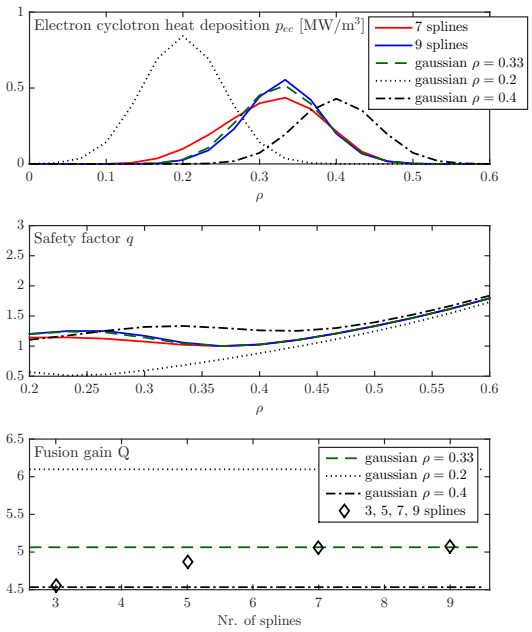

Figure 9. q **profile tailoring with EC deposition** The optimization problem is solved on several spline bases, with an increasing number of splines, hence increasing the degrees of freedom available to fine-tune the radial electron cyclotron deposition profile. Increasing the number of splines above 7 has a minor impact on the resulting maximum fusion gain Q. The figure also presents the performance of the stationary states corresponding to electron cyclotron deposition modeled as a single fixed-width gaussian (width $\Delta\rho = 0.15$), with deposition location at $\rho_{ec} = 0.2$, $\rho_{ec} = 0.33$ (optimum) and $\rho_{ec} = 0.4$.

gains Q.

Further insight is gained by formulating the optimization problem in terms of a single optimization variable: the deposition location of a fixed-width gaussian (width $\Delta\rho = 0.15$). The resulting optimum ($\rho_{ec} = 0.33$) illustrates that a single degree of freedom is sufficient to retrieve the optimum q profile, i.e. the q profile impinging $q = 1$ at the outermost radius that can be achieved with the available electron cyclotron resources. In addition to this optimum, Figure 9 also illustrates the q profiles that result from depositing the electron cyclotron current drive further outward ($\rho_{ec} = 0.4$) or inward ($\rho_{ec} = 0.2$). Deposition further out clearly results in a sub-optimal situation: the available electron cyclotron power is not sufficient to pin the q profile down to $q = 1$ (note that the electron cyclotron current drive efficiency degrades when moving to larger radii), resulting in a reduced magnetic shear at outer radii, yielding $Q \sim 4.5$. Although deposition of the electron cyclotron waves further inward results in an increased shear at outer radii, yielding $Q \sim 6.1$, the $q > 1$ constraint is violated.

To check the impact of the assumed deposition width, the optimizer is run with different settings for the width of the gaussian, in a range $\Delta\rho = 0.1 - 0.3$. Reducing the width allows an increase of s/q around mid-radius, improving the confinement enhancement. However, for $\Delta\rho < 0.2$, the fusion gain increase that can be achieved by further reducing $\Delta\rho$ turns out to be negligible.

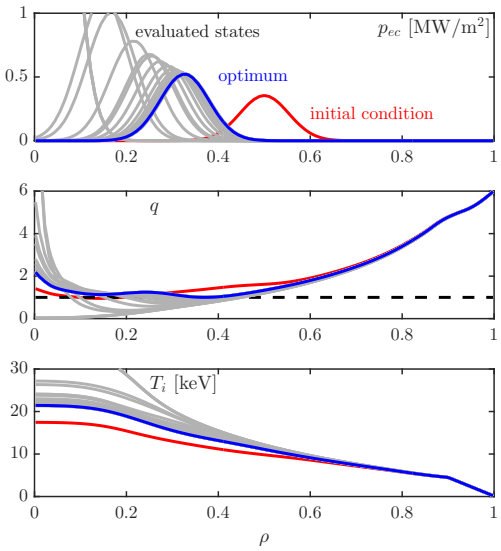

Figure 10. Optimizer iteration steps The heat deposition profile p_{ec}, q profile and T_i profile for every stationary plasma state which the optimization routine has visited are shown.

Now that the consequences of an increase and decrease of the electron cyclotron deposition radius are understood, it is instructive to visualize subsequent optimizer iteration steps. Figure 10 shows the heat deposition profile and corresponding q and T_i profiles for every stationary plasma state for which the cost function is evaluated. From the initial deposition radius at $\rho_{ec} = 0.5$, a clear confinement increase can be achieved by reducing ρ_{ec}. As the optimizer overshoots into the infeasible operating space with $q < 1$, the constraint gradient guides the state back, by increasing ρ_{ec} until $q > 1$.

Simple manipulation of the neural networks can give understanding in the transport physics effects at play when moving ρ_{ec} inward. On the one hand one can expect the $T_{e,i}$ profiles to rise as a result of the increased heat flux passing at low radii (heat flux $q_{e,i} \sim \chi_{e,i} \frac{\partial T_{e,i}}{\partial \rho}$). Due to the stiffness characterizing plasma turbulence, this effect is anticipated to be secondary compared to the impact of the increased s/q (beyond mid-radius) on the ITG threshold. This can be illustrated as follows: the stationary solution for the optimum $\rho_{ec} = 0.33$ can be recalculated while feeding the q and s profile corresponding to the stationary state solution with $\rho_{ec} = 0.5$ to the neural networks. In this way the effect of q profile tailoring is neutralized. The result is presented in Figure 11. The profiles corresponding to the stationary state attained for $\rho_{ec} = 0.5$ are shown in red, while the stationary state reached for the optimum $\rho_{ec} = 0.33$ is represented in blue. The green profiles show the temperatures and thermal diffusivities achieved when depositing the electron cyclotron waves at $\rho_{ec} = 0.33$, but providing the s and q profiles of the $\rho_{ec} = 0.5$ simulation to the respective neural network inputs. There is virtually no change in the ion temperature T_i (and hence Q) between the red and the green profiles. Although the ion heat flux passing through $\rho \sim 0.33$ is increased through electron-ion equipartitioning, this effect is counteracted by an increased ion heat diffusivity χ_i. Note that the electron temperature profile behaves notably less stiff. However, when the consistent s and q profiles are fed to the neural network, an ion energy confinement enhancement is observed. A rise in

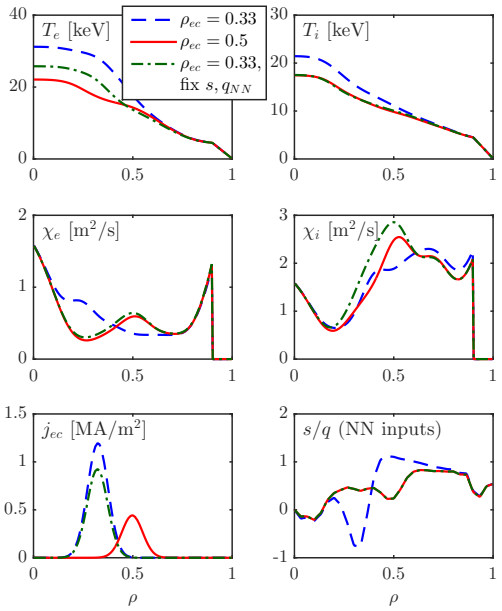

Figure 11. Impact q profile tailoring on transport The profiles corresponding to the stationary state attained for $\rho_{ec} = 0.5$ are shown in red, while the stationary state reached for the optimum $\rho_{ec} = 0.33$ is represented in blue. The green profiles show the temperatures and thermal diffusivities achieved when depositing the electron cyclotron waves at $\rho_{ec} = 0.33$, but providing the s and q profiles of the $\rho_{ec} = 0.5$ simulation to the respective neural network inputs.

the ratio s/q for radii $\rho > 0.4$ results in a drop of the ion heat diffusivity around mid-radius, resulting in a distinct rise of both T_i and T_e. Since the temperature equations are not solved within the pedestal region, the local diffusivities are not evaluated for $\rho > 0.9$.

4.3. Scan over optima at different total plasma current

The previous section illustrated how the optimization of the deposition location of a single fixed-width gaussian suffices to have the q profile clamped to $q = 1$ as far radially out as possible for a given total electron cyclotron power ($P_{ec} = 40\,\mathrm{MW}$), resulting in maximized fusion gain Q with $q > 1$ for fixed total plasma current ($I_p = 10.5\,\mathrm{MA}$), neutral beam power deposition profiles ($P_{nb} = 33\,\mathrm{MW}$, $p_{nb\ e,i}(\rho)$, $j_{nb}(\rho)$) and plamsa density profile ($n_e(\rho)$ with $\langle n_e \rangle_{line}/n_{e\ Gw} = 0.9$ and $n_{e,0}/n_{e\ ped} = 1.4$). This section presents scans over operation points in a total plasma current range bounded on the low side by fully non-inductive operation $I_p = I_{ni}$ and on the high side by the maximum I_p for which $q > 1$ can be sustained (for given density profile and auxiliary powers). Note that operation at lower Greenwald density fraction allows operation at higher plasma currents due to the increased current drive efficiency of auxiliary heating systems.

This scan is repeated at two levels of neutral beam total power injection, respectively 33 MW and 16.5 MW. For each value of I_p and P_{nb}, the optimization routine finds the electron cyclotron deposition location ρ_{ec} maximizing fusion gain Q, assuming fixed total auxiliary powers ($P_{nb} = 33/16.5\,\mathrm{MW}$ and $P_{ec} = 40\,\mathrm{MW}$), while ensuring $q > 1$. Electron density, neutral

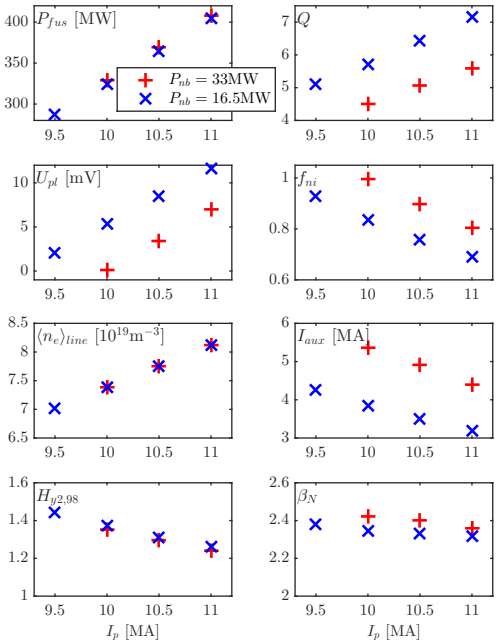

Figure 12. Optimize ρ_{ec} to maximize Q with q > 1 for various I_p and a fixed heating mix Key performance indicators are shown for the operation points maximizing fusion gain Q, assuming fixed total auxiliary powers ($P_{nb} = 33/16.5$ MW and $P_{ec} = 40$ MW), while ensuring $q > 1$, with the electron cyclotron deposition location ρ_{ec} as single optimization variable.

I_p	ρ_{ec}	P_{fus}	P_{aux}	I_{aux}	Q	U_{pl}	f_{ni}	f_{bs}	$H_{y2,98}$	β_N
[MA]		[MW]	[MW] nb + ec	[MA]		[mV]				
10	0.31	326	33+40	5.3	4.5	0.5	0.98	0.45	1.4	2.4
10.5	0.33	367	33+40	4.8	5.0	3.7	0.89	0.43	1.3	2.4
11	0.34	404	33+40	4.3	5.5	7.4	0.80	0.40	1.2	2.4

Table 2. Optimize ρ_{ec} to maximize Q with q > 1 for various I_p and a fixed heating mix ($P_{nb} = 33$MW) Key performance indicators are shown for the operation points maximizing fusion gain Q, assuming fixed total auxiliary powers ($P_{nb} = 33$ MW and $P_{ec} = 40$ MW), while ensuring $q > 1$, with the electron cyclotron deposition location ρ_{ec} as single optimization variable.

beam deposition and line radiation profiles are modeled as outlined in Section 4.1, rendering those profile values simple linear functions of the total plasma current I_p. The fusion gain can be further enhanced at given total plasma current and neutral beam power, by reducing the total electron cyclotron power P_{ec}. The resulting two-dimensional optimization problems are presented in Section 4.4.

Key physical quantities and performance indicators of the optimal scenarios, obtained at

I_p	ρ_{ec}	P_{fus}	P_{aux}	I_{aux}	Q	U_{pl}	f_{ni}	f_{bs}	$H_{y2,98}$	β_N
[MA]		[MW]	[MW] nb + ec	[MA]		[mV]				
9.5	0.29	283	16.5+40	4.2	5.0	2.4	0.92	0.48	1.4	2.4
10	0.30	322	16.5+40	3.8	5.7	5.5	0.83	0.45	1.4	2.3
10.5	0.32	363	16.5+40	3.5	6.4	8.7	0.75	0.42	1.3	2.3
11	0.33	402	16.5+40	3.2	7.1	12.0	0.68	0.40	1.3	2.3

Table 3. Optimize ρ_{ec} to maximize Q with $q > 1$ for various I_p and a fixed heating mix ($P_{nb} = 16.5$MW) Key performance indicators are shown for the operation points maximizing fusion gain Q, assuming fixed total auxiliary powers ($P_{nb} = 16.5$ MW and $P_{ec} = 40$ MW), while ensuring $q > 1$, with the electron cyclotron deposition location ρ_{ec} as single optimization variable.

different values of I_p, are summarized in Figure 12 ($P_{nb} = 16.5/33$ MW), Table 2 ($P_{nb} = 33$ MW) and Table 3 ($P_{nb} = 16.5$ MW). The electron cyclotron deposition location ρ_{ec} is indicated for each of the scenarios in Table 2 and Table 3. Note that although this optimization variable only varies modestly between the various optima, it is clear that an increased plasma current I_p requires the deposition of the electron cyclotron current drive at larger radii to avoid the q profile to drop below $q = 1$.

For a given total auxiliary power P_{aux}, the increase of plasma current I_p allows an increase of the produced fusion power P_{fus} (and hence an increase of $Q = P_{fus}/P_{aux}$), at the expense of an increased need for inductive current drive (increase of the loop voltage U_{pl}), ultimately limiting the burn phase duration. The achievable burn phase duration is dependent on the flux swing available during the flat-top discharge phase, i.e. the total available central solenoid flux charge ($\psi_0 = 240$ Wb) minus the flux swing consumption during ramp-up. Although the latter is dependent on the ramp-up scenario, a simple estimate is given in [25]: $\Delta\psi_{ramp} = 14 I_p$. These numbers allow to calculate an approximate value for the loop voltage required for operation over $t_{burn} = 3000s$ at $I_p = 11$ MA:

$$U_{pl\ required} = \frac{\psi_0 - \Delta\psi_{ramp}}{t_{burn}} = 29\,\mathrm{mV} \tag{18}$$

This value is higher than any of the stationary state loop voltages obtained in this section. This indicates that any scenario presented in this section can in principle be sustained for the full time window available for an ITER discharge.

The ion core temperatures do not vary significantly over the considered I_p range. This leads to an increasingly large energy confinement enhancement compared to the H98(y,2) scaling law for reducing total plasma current I_p. Improved pedestal confinement for higher plasma current is accounted for by the linear pedestal pressure height increase with I_p. Nevertheless, QLKNN predicts an improved overall core confinement enhancement for reduced I_p, as confirmed by the $H_{y2,98}$ factors in Table 2 and 3 and Figure 12. The fusion power hence increases with I_p due to the linear increase of the density profiles with I_p (at constant Greenwald fraction). An increased plasma current I_p requires increased inductive current drive $I_{ind} = I_p - I_{aux} - I_{bs}$. This is not solely due to the higher total current requirement, but also because of the degrading efficiency of auxiliary current drive at higher densities (i.e. decreasing I_{aux}). A fusion gain of $Q = 4.5$ is modeled at virtually steady state conditions for $I_p = 10$ MA and $P_{nb} = 33$ MW. The density increase facilitated by increasing the plasma current to 11 MA results in a fusion gain increase of more than 20%, to $Q = 5.5$, while the non-inductive current fraction drops to

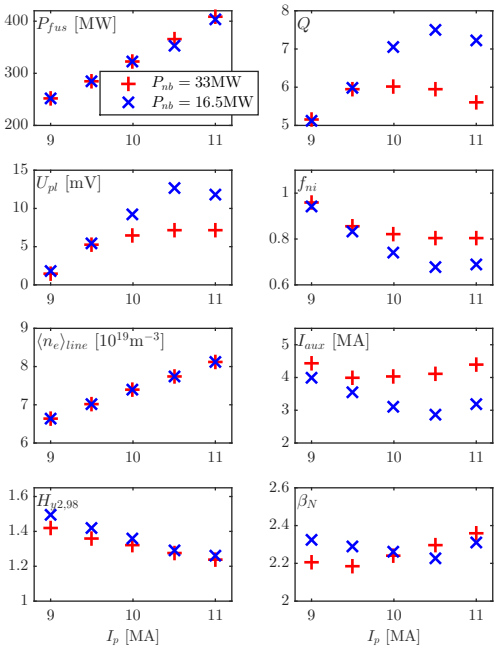

Figure 13. Optimize ρ_{ec} and P_{ec} to maximize Q with $q > 1$ and $P_{sep} > 1.2P_{LH}$ for various I_p Key performance indicators are shown for the operation points maximizing the fusion gain Q with $q > 1$ and $P_{sep} > 1.2P_{LH}$ for given plasma current and neutral beam power $P_{nb} = 33/16.5$ MW, optimizing the electron cyclotron heating power P_{ec} and deposition location ρ_{ec}.

$f_{ni} = 0.80$, requiring a loop voltage $U_{pl} = 7.4$ mV.
Comparing the optima for both levels of neutral beam power 33 MW and 16.5 MW, it is clear that a reduced beam power benefits the fusion gain, although the reduced amount of auxiliary driven current needs to be compensated by an increased inductive current drive (loop voltage U_{pl}). The optimized off-axis electron cyclotron current drive allows the formation of similar hybrid scenario q profiles for either $P_{nb} = 33$ MW or 16.5 MW, resulting in a similar energy confinement enhancement ($H_{y2,98}$ factors on Figure 12). The increased heat flux passing through the plasma barely impacts the fusion power density due to the stiffness of the ion temperature profile. As a result, similar total fusion powers P_{fus} can be achieved with less auxiliary resources P_{aux}, giving fusion gains in the range $Q = 5.0 \rightarrow 7.1$, while $U_{pl} = 2.4\,\text{mV} \rightarrow 12.0\,\text{mV}$ and $f_{ni} = 0.92 \rightarrow 0.68$. Furthermore, for steady state operation with $P_{nb} = 16.5$ MW, the plasma current needs to be reduced below $I_p = 9.5$ MA. Although the fusion gain for this steady state scenario is still around 5, the resulting fusion power drops below 300 MW. Note that for all of the above scenarios $P_{sep} > 1.2P_{LH}$, where the power crossing the separatrix is $P_{sep} = P_{oh} + P_{alpha} + P_{aux} - P_{rad}$ and the HL threshold power is evaluated with the Martin scaling law [66].

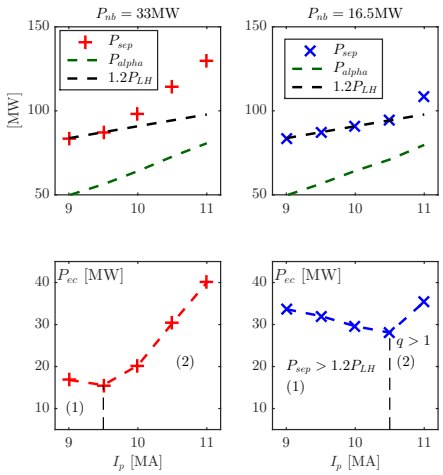

Figure 14. Active constraints when reducing P_{ec} to maximize Q with $q > 1$ and $P_{sep} > 1.2P_{LH}$ In the upper panels, the power crossing the separatrix is shown for the various optima obtained by maximizing the fusion gain Q for given plasma current and neutral beam power $P_{nb} = 33/16.5$ MW, optimizing the electron cyclotron heating power P_{ec} and deposition location ρ_{ec}. The $P_{sep} > 1.2P_{LH}$ constraint and alpha heating power are also shown. For scenarios at the lower end of the I_p range the feasible reduction of the electron cyclotron power is clearly limited by the P_{sep} constraint (labeled (1) in the lower panels), while the $q > 1$ constraint limits a further reduction of P_{ec} on the higher end of the I_p range (labeled (2) in the lower panels).

4.4. Optimization of the heating mix

4.4.1. Neutral beam and electron cyclotron power The previous section illustrates how both an increase of total plasma current and a reduction of neutral beam power give rise to an increasing fusion gain Q at the expense of a reduced maximum burn phase duration $t_{burn} \sim 1/U_{pl}$ (for a fixed electron cyclotron power P_{ec}). This result provokes the question whether a further increase of Q can be achieved by reducing the electron cyclotron heating power. This can be investigated quantitatively by formulating an optimization problem in terms of two optimization variables: electron cyclotron deposition location ρ_{ec} and total electron cyclotron power P_{ec}. The optimization objective is the maximization of the fusion gain Q, while satisfying the constraint $q > 1$. An additional constraint is added to ensure that the power crossing the separatrix P_{sep} remains more than 20% in excess of the HL threshold power P_{LH} [66]: $P_{sep} > 1.2P_{LH}$. Figure 13 ($P_{nb} = 16.5/33$ MW), Table 4 ($P_{nb} = 33$ MW) and Table 5 ($P_{nb} = 16.5$ MW) present salient performance indicators of the resulting optimized scenarios, as well as the obtained values for the optimization variables ρ_{ec} and P_{ec}.
Comparing Table 4 to Table 2 and Table 5 to Table 3, a reduction of the electron cyclotron power indeed results in an increase of the fusion gain Q. The reduction of electron cyclotron current drive needs to be compensated by an increased loop voltage driving inductive current. Due to ion temperature profile stiffness, the heating power reduction only moderately affects the produced fusion power, as long as the current drive capability is sufficient to maintain $q > 1$. The increase of Q which can be achieved depends on the magnitude of the decrease of the electron cyclotron power. Depending on the value of the total plasma current, the feasible reduction of the electron cyclotron power is limited by one of the following constraints.

- The current density profiles of scenarios at the *higher end of the I_p range* have a

I_p	ρ_{ec}	P_{fus}	P_{aux}	I_{aux}	Q	U_{pl}	f_{ni}	f_{bs}	$H_{y2,98}$	β_N
[MA]		[MW]	[MW] nb + ec	[MA]		[mV]				
9	0.25	249	33+17	4.4	5.0	1.3	0.96	0.47	1.4	2.2
9.5	0.26	281	33+16	4.0	5.8	5.1	0.86	0.44	1.4	2.2
10	0.29	321	33+20	3.9	6.0	6.8	0.81	0.42	1.3	2.2
10.5	0.32	364	33+30	4.2	5.7	6.8	0.81	0.41	1.3	2.3
11	0.34	404	33+40	4.3	5.5	7.4	0.80	0.40	1.2	2.4

Table 4. Optimize ρ_{ec} and P_{ec} to maximize Q with $q > 1$ and $P_{sep} > 1.2P_{LH}$ for various I_p ($P_{nb} = 33$MW) Key performance indicators are shown for the operation points maximizing the fusion gain Q with $q > 1$ and $P_{sep} > 1.2P_{LH}$ for given plasma current I_p and neutral beam power $P_{nb} = 33$ MW, optimizing the electron cyclotron heating power P_{ec} and deposition location ρ_{ec}.

I_p	ρ_{ec}	P_{fus}	P_{aux}	I_{aux}	Q	U_{pl}	f_{ni}	f_{bs}	$H_{y2,98}$	β_N
[MA]		[MW]	[MW] nb + ec	[MA]		[mV]				
9.0	0.27	248	16.5+34	4.1	5.0	1.5	0.95	0.50	1.5	2.3
9.5	0.28	283	16.5+32	3.6	5.8	5.2	0.84	0.46	1.4	2.3
10	0.29	321	16.5+30	3.1	7.0	9.1	0.74	0.43	1.4	2.3
10.5	0.31	355	16.5+28	2.7	7.9	13.3	0.66	0.40	1.3	2.2
11	0.33	399	16.5+35	2.9	7.6	13.7	0.65	0.39	1.3	2.3
11	0.33	396	0+42	2.1	9.4	16.5	0.58	0.39	1.3	2.3

Table 5. Optimize ρ_{ec} and P_{ec} to maximize Q with $q > 1$ and $P_{sep} > 1.2P_{LH}$ for various I_p ($P_{nb} = 16.5$MW) Key performance indicators are shown for the operation points maximizing the fusion gain Q with $q > 1$ and $P_{sep} > 1.2P_{LH}$ for given plasma current I_p and neutral beam power $P_{nb} = 16.5$ MW, optimizing the electron cyclotron heating power P_{ec} and deposition location ρ_{ec}. For $I_p = 11$ MA, the optimum obtained without any neutral beam power is also presented.

comparatively larger contribution driven inductively and hence require in absolute terms more off-axis non-inductive current drive to maintain $q > 1$, limiting the feasible P_{ec} reduction. Since this effect dominates the increase of fusion power for increased plasma current (due to increased density), *an increase of I_p leads to a decreasing fusion gain Q.*

- For scenarios at the *lower end of the I_p range* the feasible reduction of the electron cyclotron power is limited by the P_{LH} constraint. This is clearly illustrated in Figure 14, where the power crossing the separatrix and the constraining lower value are shown for the different scenarios. Although the required threshold power P_{LH} decreases for reduced plasma current I_p (due to reduced density), this does not lead to a reduction of the required total auxiliary power since fusion power is essentially proportional to the square of the density and the plasma self-heating due to fusion-born alphas hence strongly diminishes (also shown in Figure 14). Within this range, *an increase of I_p allows for an increasing fusion gain Q.*

Due to these counteracting considerations, the achievable increase for the fusion gain Q is most pronounced for intermediate plasma currents, as illustrated in Figure 13 and Figure

14. For those scenarios where the separatrix power constraint is not active, the loop voltage U_{pl} is virtually constant due to the counteracting effects of increasing total current and reducing current drive efficiency on the one hand and an increased level of maintained electron cyclotron current drive.
It might be surprising to notice that for $I_p = 11\,\mathrm{MA}$ (where the P_{LH} constraint is not active), a lower level of electron cyclotron power is required to maintain $q > 1$ when decreasing the neutral beam power power from $P_{nb} = 33\,\mathrm{MW}$ to $P_{nb} = 16.5\,\mathrm{MW}$ (the required electron cyclotron power decreases from $P_{ec} = 40\,\mathrm{MW}$ to $P_{ec} = 35\,\mathrm{MW}$). Note that violation of the $q > 1$ constraint at low radii is dependent on the particular shape of $j_{oh} + j_{bs} + j_{nb}$, which strongly depends on the imposed neutral beam and density profiles. Since the peak of the neutral beam current density profile is relatively close to the magnetic axis in the present simulations, a reduced neutral beam power can relax the required amount of off-axis electron cyclotron current to maintain $q > 1$.
Finally, one might consider a further reduction of the neutral beam power down to zero. Looking for a maximum fusion gain Q, with $q > 1$ and $P_{sep} > 1.2P_{LH}$, an optimum is found with $P_{ec} = 42\,\mathrm{MW}$ (see final row Table 5). For the selected density, an electron cyclotron power slightly in excess of the upgraded electron cyclotron power capability is required in absence of any neutral beam power. Although a high fusion gain $Q = 9.4$ is projected, a major contribution of inductive current drive is required ($U_{pl} = 16.5\,\mathrm{mV}$ and $f_{ni} = 0.58$). Note that scenarios without neutral beam injection at lower plasma current would require a further increase of the electron cyclotron power to maintain $P_{sep} > 1.2P_{LH}$, due to the reducing alpha heating.
In conclusion, the fusion power is only modestly impacted by the additional heat flow caused by auxiliary heating, due to the stiffness of the ion temperature profile. Upper limits for the fusion gain Q are hence set by either minimum power requirements for the separatrix power flow to maintain H-mode or by minimum current drive requirements for q profile tailoring.

4.4.2. ITER baseline heating mix Many of the above simulations assume the availability of 40 MW electron cyclotron power on ITER. In the present section a brief assessment is made of the hybrid scenario performance that can be achieved with the baseline heating mix foreseen for ITER, including 33 MW of neutral beam power, 20 MW of electron cyclotron power and 20 MW of ion cyclotron power [44]. For a given total plasma current I_p, one can envisage two pathways to reduce electron cyclotron heating in the presence of the $q > 1$ and P_{LH} constraints.

- The available ion cyclotron heating power can contribute to the required power flow across the separatrix.
- A reduction of the density, accompanied by a simultaneous increase of temperature pedestal to maintain identical pedestal pressure, renders both constraints less stringent: (1) maintaining $P_{sep} > 1.2P_{LH}$ requires less electron cyclotron power because the decrease of P_{LH} for reducing density dominates the decrease of alpha heating (the effect of reducing density is partly counteracted by an increasing ion temperature pedestal¶.); (2) maintaining $q > 1$ requires less electron cyclotron power because of the increase in current drive efficiency.

To quantify the potential of these pathways, an optimization problem is constructed in terms of three optimization variables: electron cyclotron deposition location ρ_{ec}, total plasma current I_p and ion cyclotron heating power P_{ic}. Ion cyclotron heating is modeled as a gaussian

¶ For low core temperatures ($T_i \sim 15 - 20\,\mathrm{keV}$), the fusion cross-section scales with $(n_e T_i)^2$; the exponent of the T_i dependence however diminishes for higher temperatures [52]

f_{Gw}	I_p	ρ_{ec}	P_{fus}	P_{aux}	I_{aux}	Q	U_{pl}	f_{ni}	f_{bs}
	[MA]		[MW]	[MW] nb + ec + ic	[MA]		[mV]		
0.9	9.6	0.27	286	0+20+29	1.2	5.8	15.1	0.57	0.44
0.8	10.2	0.29	306	0+20+19	1.4	7.8	14.3	0.55	0.42
0.9	10.1	0.28	321	16.5+20+11	2.5	6.7	12.8	0.66	0.42
0.8	10.6	0.31	341	16.5+20+1	2.8	9.1	12.0	0.65	0.39
0.9	10.0	0.29	319	33+20+0	3.9	6.0	6.8	0.81	0.42
0.8	10.5	0.31	339	33+20+0	4.5	6.4	5.5	0.83	0.40

Table 6. Heating mix Key performance indicators are shown for the operation points maximizing the fusion gain Q with $q > 1$ and $P_{sep} > 1.2P_{LH}$ by optimizing electron cyclotron deposition location ρ_{ec}, total plasma current I_p and ion cyclotron heating power P_{ic} (for given neutral beam power $P_{nb} = 0/16.5/33\,\mathrm{MW}$, electron cyclotron power $P_{ec} = 20\,\mathrm{MW}$ and density $\frac{\langle n_e \rangle_{line}}{n_{e\ Gw}} = 0.9$ and 0.8).

centered on the magnetic axis with width $\Delta\rho = 0.2$, depositing equal amounts of power to ions and electrons[+]. The goal is once more maximizing the fusion gain Q with $q > 1$ and $P_{sep} > 1.1P_{LH}$. The optimization is executed for three levels of neutral beam power ($P_{nb} = 0/16.5/33\,\mathrm{MW}$) in combination with two different densities ($\frac{\langle n_e \rangle_{line}}{n_{e\ Gw}} = 0.9$ and 0.8), while the electron cyclotron power is set to $P_{ec} = 20\,\mathrm{MW}$. The results are summarized in Table 6. For each of the six cases, the optimizer attempts to increase the plasma current (and density) to the largest extent as feasible without violating the $q > 1$ constraint with the available 20 MW of electron cyclotron heating power. The increasing fusion power for rising density allows to reduce the ion cyclotron heating as the alpha heating contributes to the threshold separatrix power flow required to maintain H-mode. For a given neutral beam power, a reduced density (with simultaneous increase in pedestal temperature), improves the electron cyclotron current drive efficiency, hence allowing to maintain $q > 1$ for a higher plasma current (corresponding to a higher fusion gain Q). The high density case without neutral beam heating requires 29 MW of ion cyclotron power, beyond the upper limit. Lowering the line-averaged density to $\frac{\langle n_e \rangle_{line}}{n_{e\ Gw}} = 0.8$ allows increasing the plasma current to $I_p = 10.2\,\mathrm{MA}$, limiting the required ion cyclotron power below 20 MW. While the scenarios with $P_{nb} = 16.5\,\mathrm{MW}$ achieve increased plasma currents compared to the scenarios relying solely on RF wave heating and current drive, a further increase of neutral beam heating and current drive from 16.5 MW to 33 MW does not enable an increase in plasma current, illustrating once more that for neutral beam injection with a deposition profile peaked near the magnetic axis, a power increase is not necessarily beneficial for maintaining $q > 1$. However, neutral beams are clearly a key source of bulk current required to increase the fraction of non-inductively driven current. Furthermore, the two scenarios with $P_{nb} = 33\,\mathrm{MW}$ do not require additional ion cyclotron heating, as the separatrix power flow for combined neutral beam and electron cyclotron heating is in excess of $1.2P_{LH}$ ($P_{sep} - 1.2P_{LH} = 6.8\,\mathrm{MW}$ and 16.8 MW for respectively $\frac{\langle n_e \rangle_{line}}{n_{e\ Gw}} = 0.9$ and 0.8).

[+] Note that for ion cyclotron heating, the relative heating of the different plasma species depends on the applied heating scheme. These considerations are beyond the scope of the present paper. An even split between electron and ion heating for a DT plasma seems however a reasonable first-order estimate [67].

f_{Gw}	I_p	ρ_{ec}	P_{fus}	P_{aux}	I_{aux}	Q	U_{pl}	f_{ni}	f_{bs}
	[MA]		[MW]	[MW] nb + ec	[MA]		[mV]		
0.9	10.5	0.33	365	33+40	4.8	5.0	3.6	0.89	0.43
0.8	10.8	0.34	364	33+40	5.8	5.0	1.1	0.96	0.42
0.9	11.0	0.34	404	33+40	4.3	5.5	7.4	0.80	0.40
0.8	11.7	0.37	430	33+40	5.1	5.9	5.5	0.82	0.39
0.9	9.6	0.38	264	33+20	3.9	5.0	7.1	0.82	0.42
0.8	9.8	0.39	264	33+20	4.6	5.0	3.8	0.89	0.42
0.9	10.0	0.29	319	33+20	3.9	6.0	6.8	0.81	0.42
0.8	10.5	0.31	339	33+20	4.5	6.4	5.5	0.83	0.40

Table 7. Electron cyclotron power upgrade Key performance indicators are shown for the operation points constituting the vertices of the quadrangles in Figure 15. The electron cyclotron deposition location ρ_{ec} for each of these scenarios maximizes the fusion gain Q, while ensuring $q > 1$.

4.4.3. Electron cyclotron power upgrade Combining some of the trends uncovered in the previous sections, the operational windows for an ITER hybrid scenario with availability of either $P_{ec} = 20\,\text{MW}$ or $P_{ec} = 40\,\text{MW}$ (while assuming $P_{nb} = 33\,\text{MW}$ and $P_{ic} = 0\,\text{MW}$) can be compared quantitatively. The maximum plasma current for which $q > 1$ can be maintained is dependent on both the available amount of electron cyclotron power and the plasma density, as both impact the amount of off-axis current drive that can be deposited to tailor the q profile. For a given amount of injected auxiliary power, both fusion power P_{fus} and fusion gain Q increase when increasing plasma current I_p, while maintaining the fraction of the line-averaged density to the Greenwald density limit constant. The colored quadrangles in Figure 15 circumscribe the operational window with a Greenwald density fraction $f_G = \langle n_e \rangle_{line} / n_{e\,Gw}$ within the range $[0.8, 0.9]$ and a fusion gain $Q > 5$, with the availability of respectively 20 MW (blue) and 40 MW (red) of electron cyclotron power. As discussed in Section 4.1, the pedestal pressure is assumed to be linearly increasing with plasma current I_p. A density reduction at given plasma current is counteracted by a temperature pedestal increase, keeping the pedestal pressure constant. The four vertices of the quadrangles represent the scenarios with optimized electron cyclotron deposition radius, corresponding to $Q = 5$ (star symbol on the low I_p side) and the maximum I_p for which $q > 1$ can be maintained (rectangle symbol on the high I_p side). The relative levels of non-inductively driven current $f_{ni} = I_{ni}/I_p$ of these scenarios are also indicated on the figure. The $Q = 5$ scenarios with $P_{ec} = 40\,\text{MW}$ clearly achieve a higher f_{ni}, with the low density case operating close to steady state conditions. Some performance indicators of these eight scenarios are summarized in Table 7. Note that the maximum fusion gains achieved with $P_{ec} = 20\,\text{MW}$ ($Q = 6.0$ for $f_G = 0.9$ and $Q = 6.4$ for $f_G = 0.8$) are higher than the maximum fusion gains achieved with $P_{ec} = 40\,\text{MW}$ ($Q = 5.5$ for $f_G = 0.9$ and $Q = 5.9$ for $f_G = 0.8$), although the increased plasma current yields fusion powers in excess of 400 MW for the latter. The differences in fusion power P_{fus} are illustrated by a set of diagonal lines on Figure 15. In summary, one can conclude that increased electron cyclotron power resources widen the hybrid scenario operational space, allowing to achieve higher fusion power, while requiring less inductive current drive for a similar fusion gain Q.

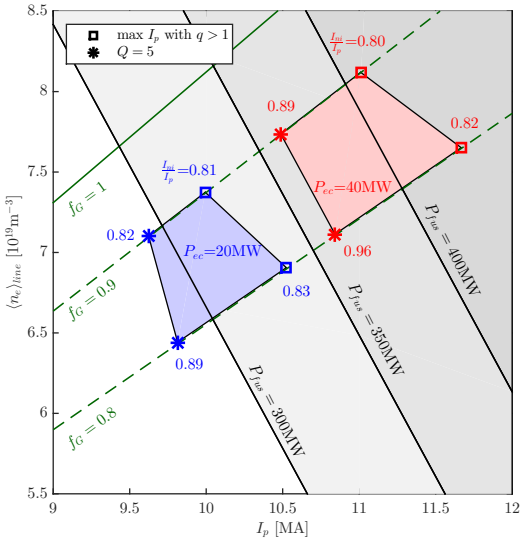

Figure 15. Electron cyclotron power upgrade The colored quadrangles circumscribe the operational window with a Greenwald density fraction $f_G = \langle n_e \rangle_{line}/n_{e\,Gw}$ within the range $[0.8, 0.9]$ and a fusion gain $Q > 5$, with the availability of respectively 20 MW (blue) and 40 MW (red) of electron cyclotron power. The four vertices of the quadrangles represent the scenarios with optimized electron cyclotron deposition location, corresponding to $Q = 5$ (star symbol on the low I_p side) and the maximum I_p for which $q > 1$ can be maintained (rectangle symbol on the high I_p side). The relative levels of non-inductively driven current $f_{ni} = I_{ni}/I_p$ of these scenarios are also indicated on the figure. The differences in fusion power P_{fus} are illustrated by a set of diagonal lines. As discussed in Section 4.1, the pedestal pressure is assumed to be linearly increasing with plasma current I_p. A density reduction at given plasma current is counteracted by a temperature pedestal increase, keeping the pedestal pressure constant.

$T_{e,i\ ped}$	ρ_{ec}	P_{fus}	P_{aux}	I_{aux}	Q	U_{pl}	f_{ni}	f_{bs}	$H_{y2,98}$	β_N
[keV]		[MW]	[MW] nb + ec	[MA]		[mV]				
3.5	0.35	273	33+45	4.7	3.5	8.6	0.79	0.35	1.1	2.0
4.5	0.32	364	33+30	4.2	5.7	6.8	0.81	0.41	1.3	2.3
5.5	0.28	448	33+18	3.6	8.8	5.6	0.83	0.48	1.4	2.5

Table 8. Pedestal pressure sensitivity (with variable P_{ec}) Key performance indicators are shown for the operation points maximizing the fusion gain Q with $q > 1$ and $P_{sep} > 1.2P_{LH}$ by optimizing both the deposition location ρ_{ec} and the power level of electron cyclotron heating P_{ec} (for given plasma current $I_p = 10.5$ MA and neutral beam power $P_{nb} = 33$ MW), for respective pedestal temperatures $T_{e,i\ ped} = 3.5$ keV, 4.5 keV and 5.5 keV.

4.5. Impact of temperature pedestal on scenario performance

Due to the stiff behaviour of the core ion temperature profile, the assumed temperature pedestal height has a strong impact on the predicted fusion power. Furthermore, the $q > 1$

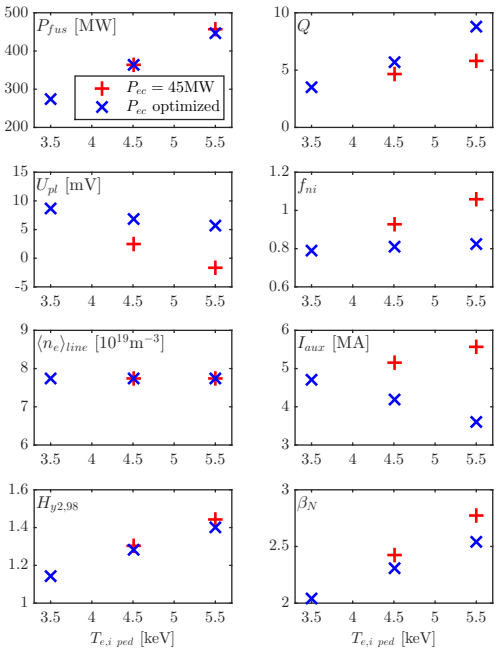

Figure 16. Pedestal pressure sensitivity Key performance indicators are shown of stationary states maximizing the fusion gain Q by optimizing both the deposition location and the power level of electron cyclotron heating (for given plasma current $I_p = 10.5$ MA and neutral beam power $P_{nb} = 33$ MW), for respective pedestal temperatures $T_{e,i\ ped} = 3.5$ keV, 4.5 keV and 5.5 keV, in addition to the respective quantities for stationary states maximizing the fusion gain Q by optimizing the deposition location (for given plasma current $I_p = 10.5$ MA, electron cyclotron heating $P_{ec} = 45$ MW and neutral beam power $P_{nb} = 33$ MW). $q > 1$ and $P_{sep} > 1.2P_{LH}$ are provided as constraints to the optimizer.

$T_{e,i\ ped}$	ρ_{ec}	P_{fus}	P_{aux}	I_{aux}	Q	U_{pl}	f_{ni}	f_{bs}	$H_{y2,98}$	β_N
[keV]		[MW]	[MW] nb + ec	[MA]		[mV]				
3.5	0.35	273	33+45	4.7	3.5	8.6	0.79	0.35	1.1	2.0
4.5	0.33	365	33+45	5.2	4.7	2.4	0.92	0.43	1.3	2.4
5.5	0.32	457	33+45	5.6	5.9	-1.6	1.06	0.53	1.4	2.8

Table 9. Pedestal pressure sensitivity (with fixed P_{ec}) Key performance indicators are shown for the operation points maximizing the fusion gain Q with $q > 1$ and $P_{sep} > 1.2P_{LH}$ by optimizing the deposition location of electron cyclotron heating (for given plasma current $I_p = 10.5$ MA, neutral beam power $P_{nb} = 33$ MW and electron cyclotron heating $P_{ec} = 45$ MW), for respective pedestal temperatures $T_{e,i\ ped} = 3.5$ keV, 4.5 keV and 5.5 keV.

constraint is less restrictive for increased pedestal temperatures, due to the increased off-axis current drive contribution by the bootstrap current driven in both core and pedestal and the enhanced electron cyclotron current drive efficiency at higher T_e.

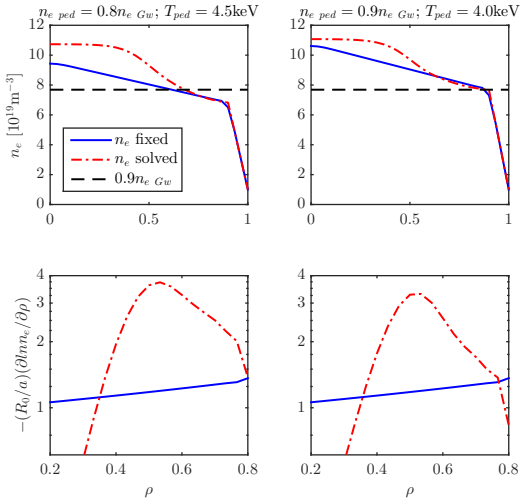

Figure 17. Density peaking A comparison is shown of the electron density profiles and electron density inverse scale length profiles considered for a sensitivity study on the impact of the Greenwald density constraint and the density peaking. For the left (right) panels, the pedestal density is respectively set to $n_{e\ ped} = 0.8n_{e\ Gw}$ ($n_{e\ ped} = 0.9n_{e\ Gw}$). The density profile is either imposed with a fixed peaking factor or solved for with QLKNN predicted transport. The fixed density profile case with $\frac{n_{e\ ped}}{n_{e\ Gw}} = 0.8$ recovers the hybrid reference case as defined earlier (with $\langle n_e \rangle_{line} = 0.9n_{e\ Gw}$).

The optimization problem of maximizing the fusion gain Q with $q > 1$ and $P_{sep} > 1.2P_{LH}$, by optimizing both the deposition location and the power level of electron cyclotron heating (for given plasma current $I_p = 10.5\,\mathrm{MA}$ and neutral beam power $P_{nb} = 33\,\mathrm{MW}$), as formulated in Section 4.4.1 and presented in Table 4, is repeated for increased and reduced temperature (and pressure) pedestal height, as presented in Figure 16 and Table 8. The result for the reference temperature pedestal ($T_{e,i\ ped} = 4.5\,\mathrm{keV}$) obtained in the previous parts, is compared to the optimum scenarios obtained for $T_{e,i\ ped} = 3.5\,\mathrm{keV}$ and $T_{e,i\ ped} = 5.5\,\mathrm{keV}$ (corresponding pedestal pressure respectively 74 kPa and 117 kPa). The elevated T_i profile for increased pedestal clearly results in more fusion power. Furthermore, the fusion gain Q is further enhanced as the required level of electron cyclotron heating can be further reduced due to the higher fraction of bootstrap current and the increased electron cyclotron current drive efficiency helping to sustain the hybrid q profile. The lowest pedestal height requires an increase of the available electron cyclotron resources to $P_{ec} = 45\,\mathrm{MW}$ to facilitate a stationary state with $q > 1$. To disentangle the dual effect on the fusion gain Q of changing both fusion power and auxiliary power, the optimizations at $T_{e,i\ ped} = 4.5\,\mathrm{keV}$ and $T_{e,i\ ped} = 5.5\,\mathrm{keV}$ are repeated with fixed levels of auxiliary power ($P_{nb} = 33\,\mathrm{MW}$ and $P_{ec} = 45\,\mathrm{MW}$), as shown in Figure 16 and Table 8.

The assumed temperature pedestal height has clearly a strong impact on the projected scenario performance, highlighting the importance of reliable pedestal stability models to predict ITER performance.

n_e	$\frac{n_{e\ ped}}{n_{e\ Gw}}$; $\frac{n_{e,0}}{n_{e\ ped}}$	P_{fus}	P_{aux}	I_{aux}	Q	U_{pl}	f_{ni}	f_{bs}	$H_{y2,98}$	β_N
		[MW]	[MW] nb + ec	[MA]		[mV]				
f	0.8; 1.4	367	33+40	4.8	5.0	3.7	0.89	0.43	1.3	2.4
s	0.8; 1.6	440	33+40	3.4	6.0	9.5	0.77	0.45	1.2	2.4
f	0.9; 1.4	377	33+40	3.5	5.1	11.2	0.74	0.41	1.2	2.3
s	0.9; 1.4	421	33+40	3.1	5.7	13.5	0.72	0.42	1.2	2.3

Table 10. Density profile sensitivity Key performance indicators are shown for four density profile scenarios with $\frac{n_{e\ ped}}{n_{e\ Gw}} = 0.8$ or 0.9 and the density profile either imposed with a fixed peaking factor ('f'=fixed) or solved for with QLKNN predicted transport ('s'=solved).

4.6. Impact of density peaking and Greenwald density limit

Since the produced fusion power strongly depends on the density, one can anticipate a strong impact of assumptions regarding the peaking of the density profile and the Greenwald density limit. The present section provides a sensitivity study on the impact on the reference case hybrid scenario of different density profiles. The modeling performed in earlier sections provided conservative predictions, considering a limited level of peaking with respect to what is expected for ITER plasmas from modeling and experiments and limiting the line-averaged density to $\langle n_e \rangle_{line} = 0.9 n_{e\ Gw}$. Assuming density limit disruptions mainly originate from phenomena close to the plasma boundary [55] (as confirmed by the observation of peaked density profiles with line-averaged densities $\langle n_e \rangle_{line} = 1.5 n_{e\ Gw}$ [68]), one could release the conservative constraint $\langle n_e \rangle_{line} = 0.9 n_{e\ Gw}$ to a constraint on the pedestal density, i.e. $n_{e\ ped} = 0.9 n_{e\ Gw}$.
The different density profiles considered in this section are presented in Figure 17.

- For the left and right panels, the pedestal density is respectively set to $n_{e\ ped} = 0.8 n_{e\ Gw}$ and $n_{e\ ped} = 0.9 n_{e\ Gw}$. The temperature pedestal is adjusted to keep the pedestal pressure unchanged. This can be motivated by the results from EPED1 modeling reported in [51], where for SOLPS consistent separatrix densities and moderate pedestal densities, the predicted pressure pedestal height is independent of the density pedestal height.
- The density profile is either imposed with a fixed peaking factor or solved for with QLKNN predicted transport. The fixed density profile case with $\frac{n_{e\ ped}}{n_{e\ Gw}} = 0.8$ recovers the hybrid reference case as defined earlier (with $\langle n_e \rangle_{line} = 0.9 n_{e\ Gw}$). Adding the electron density equation to the set of stationary diffusion equations solved by the stationary state solver in RAPTOR, QLKNN provides a prediction of the turbulence-driven inward pinch. Similarly as for the heat transport discussed earlier, the shear input of the neural network is transformed to $s - 0.5\alpha$ and only the ITG prediction is used. Note that these density peaking predictions miss the impact of TEM turbulence [61], as well as the electromagnetic effects described in [69], shown to reduce density peaking for ITER and DEMO [52]. Despite these model deficiencies, the presented density profiles provide a sensitivity study on the impact of the level of density peaking on hybrid scenario performance. Note that pellets will fuel the peripheral ITER plasma, providing effectively an actuator for the pedestal density $n_{e\ ped}$. In the present section, two levels of $n_{e\ ped}$ are compared. A further systematic study of $n_{e\ ped}$ as an optimization variable (acting hence as a proxy for the pellet fueling rate) is left for future work.

Performance indicators of the four resulting scenarios are compared in Table 10. Let us first compare the two scenarios with imposed density profiles ('f' in Table 10) and a fixed density peaking factor ($n_{e0}/n_{e\ ped} = 1.4$), with the pedestal density respectively $\frac{n_{e\ ped}}{n_{e\ Gw}} = 0.8$ and 0.9. Since the increase in pedestal density is compensated by a pedestal temperature reduction, lowering the stiff ion temperature profile rigidly, the total fusion power is only impacted modestly. For a fixed pedestal pressure and a fixed density peaking, the fusion gain is weakly dependent on the relative heights of temperature and density pedestal. The loop voltage on the other hand increases by more than a factor three due to the density increase. This is easily explained by the reduced amount of current driven non-inductively due to degrading current drive efficiency, in addition to the increasing plasma resistivity and reducing bootstrap current (lower T_i, and lower T_e/T_i for increased density).
Inspecting the QLKNN predicted density profiles in Figure 17, it is clear that the peaking is strongly impacted by the varying pedestal boundary conditions for temperature and density. Increasing the pedestal density from $n_{e\ ped} = 0.8 n_{e\ Gw}$ to $0.9 n_{e\ Gw}$, while decreasing the pedestal temperature from $T_{e,i\ ped} = 4.5\,\mathrm{keV}$ to $4.0\,\mathrm{keV}$ as to maintain a constant pedestal pressure, the predicted level of peaking decreases from $\frac{n_{e,0}}{n_{e\ ped}} = 1.6$ to 1.4. The density profile hence becomes more peaked for reducing collisionality, as expected from theory and experiment [53], [54].
For the low pedestal density cases ($\frac{n_{e\ ped}}{n_{e\ Gw}} = 0.8$; left panels Figure 17), the QLKNN predicted density profile is notably more peaked compared to the imposed density profile (confirming that $\frac{n_{e,0}}{n_{e\ ped}} = 1.4$ is a conservative assumption). The peaked density profile results in a significant increase of fusion power, and hence fusion gain ($Q = 5.0 \rightarrow 6.0$), while an increased inductive current drive is required ($U_{pl} = 3.7\,\mathrm{mV} \rightarrow 9.5\,\mathrm{mV}$; $f_{ni} = 0.89 \rightarrow 0.77$). These effects are less pronounced for the high density pedestal cases, since the predicted peaking factor is smaller. Note however that even for similar peaking factor, the radial profile of $n_e(\rho)$ can impact the produced fusion power and local current drive efficiency. Comparing finally the two scenarios with solved density profiles ('s' in Table 10), we see that increasing the pedestal density leads to a slight reduction of fusion power due to the predicted drop in density peaking (fusion gain $Q = 6.0 \rightarrow 5.7$). The inductive current drive requirement however increases ($U_{pl} = 9.5\,\mathrm{mV} \rightarrow 13.5\,\mathrm{mV}$; $f_{ni} = 0.77 \rightarrow 0.72$).
In conclusion, operation at reduced pedestal density appears favorable for the hybrid scenario, under the assumption of an equal pedestal pressure. The increased level of density peaking anticipated for smaller collisionality further reinforces this trend.

5. Conclusion

A framework for fast, automated optimization of the stationary phase of tokamak plasma discharges is presented. The RAPTOR transport code is extended with a new solution method allowing to directly obtain the stationary solution of a set of coupled, non-linear diffusion equations, for a selected number of transport channels. Cost and constraint functions, reflecting respectively plasma performance indicators and limitations on the desired plasma state, can be generically implemented. Both scalar variables (e.g. heating powers) and radially distributed quantities (e.g. electron cyclotron deposition profile) can be optimized. The stationary state solver and the non-linear programming optimization algorithm profit from the availability of analytic Jacobians within RAPTOR, yielding swift convergence, even in conjunction with a stiff transport model. The QLKNN-hyper-10D transport model [15], trained to emulate QuaLiKiz turbulent flux predictions [16], [17], is applied within the presented optimization scheme to provide first-principle-based predictions of sets of

optimized operation points for the ITER hybrid scenario. These optimization problems are typically solved within minutes on standard hardware. The impact of a consistent MHD equilibrium geometry on the transport solutions is generally minor, but can be routinely checked with an automated iterative scheme coupling RAPTOR and the CHEASE fixed boundary equilibrium solver [57].

The present study confirms that improved energy confinement relative to the H98(y,2) scaling law can be achieved in ITER, by optimizing the electron cyclotron current drive deposition location, pursuing a hybrid scenario q profile with $q > 1$ and maximizing the s/q at radii $\rho > 0.4$. Due to the lack of electromagnetic and fast ion effects in QLKNN, the confinement levels could be systematically under-predicted. Regarding core confinement the presented results can hence be considered as conservative. Note however that the trends seen in ECCD deposition modification and impact of s/q on ITG thresholds hold regardless of the electromagnetic and fast ion effects. As depositing all the available electron cyclotron power in a specific location is shown to be the optimal choice to achieve such q profile, no excessive fine-tuning of electron cyclotron deposition profile is required. For a gaussian deposition profile it suffices to find how close to the magnetic axis the deposition location can be without violating $q > 1$, having the q profile clamped to $q = 1$ at the outermost location that can be achieved for a given electron cyclotron power.

Using this novel combination of tools, ITER hybrid scenarios are projected to be a reliable avenue for long-pulse burning plasmas, with a heating mix $P_{nb} = 33\,\mathrm{MW}$ and $P_{ec} = 40\,\mathrm{MW}$ allowing for $Q = 5$ with $f_{ni} = 0.89$ and $P_{fus} = 365\,\mathrm{MW}$ (assuming $T_{e,i\ ped} = 4.5\,\mathrm{keV}$, $f_G = 0.9$ and $n_{e0}/n_{e\ ped} = 1.4$, and for $I_p = 10.5\,\mathrm{MA}$). A reduced electron cyclotron power $P_{ec} = 20\,\mathrm{MW}$ requires operation at reduced plasma current $I_p = 9.6\,\mathrm{MA}$ and achieves $Q = 5$ at $f_{ni} = 0.82$ and $P_{fus} = 264\,\mathrm{MW}$. Raising the total plasma current allows to reach a higher fusion gain Q, at the expense of an increased loop voltage U_{pl} (and hence reduced f_{ni}), as presented quantitatively in this work. The stiff behaviour of the ion temperature profile allows to further enhance the achieved fusion gain Q by reducing the amount of injected heat. Depending on the levels of total plasma current and neutral beam power, the reduction of electron cyclotron heating and current drive is either limited by the need for enough off-axis current to maintain $q > 1$, or by the need for a sufficient separatrix power flow to maintain H-mode operation, giving rise to an intermediate plasma current maximizing the fusion gain Q. Although lowering neutral beam power allows a further increase in fusion gain Q, the neutral beams are an important source of auxiliary current drive, required to reach high fractions of non-inductively driven current. Actual scenario performance is strongly dependent on the pedestal pressure and the peaking of the density profile, both having a major impact on fusion power, current drive efficiency and bootstrap current. For a given total pedestal pressure, a lowered pedestal density is favorable: fusion power is only moderately affected due to the simultaneous increase of the stiff ion temperature profile (especially when considering a more peaked density profile can be obtained at reduced collisionality), while current drive efficiency, bootstrap current and plasma conductivity are enhanced by reduced density and increased electron temperature.

Avenues to enhance the predictive capabilities of RAPTOR simulations include the continued integration of reduced-physics modules for auxiliary heating and current drive, impurity radiation, pedestal height and impurity and fast particle content. A new module evaluating impurity radiation based on ADAS cooling factor data was recently integrated in RAPTOR, while new generations of neural network emulations of the QuaLiKiz transport model, including characteristics of turbulent transport physics in the network architecture, are under development [70]. The coupling of the RABBIT code [71] is envisioned, allowing fast evaluation of neutral beam deposition profiles of heat, current and fast ions. The reliability of

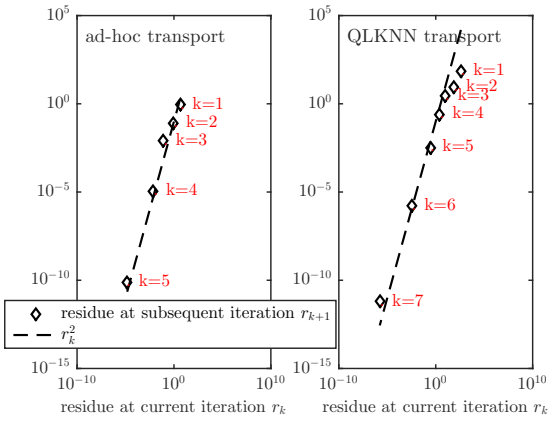

Figure A1. Convergence stationary state solver Quadratic convergence of the RAPTOR stationary state solver is illustrated, both with simple ad-hoc transport model and with neural network surrogate transport model QLKNN-hyper-10D.

the ITER hybrid operation space predictions will be improved by including the modeling of particle transport and neutral beam deposition, allowing to solve self-consistently the non-linear coupling between neutral beam deposition profiles, density peaking and thermal confinement. The evaluation of limits regarding fast particle and MHD instabilities could be included as constraints in the optimization framework. Other dynamic interactions which demand an integrated description are the interplay of (heavy) impurity transport and radiation and the impact of scrape-off layer conditions on the pedestal formation, as well as the non-linear interaction of pedestal and core confinement.
The high computational speed of the optimization scheme presented here naturally lends itself to applications where speed and rapid iterations are important, for example within reactor design system codes or for inter-shot discharge optimization.

Appendix A. Convergence studies

The Newton-Raphson solver of the RAPTOR stationary state solver converges quadratically to the root of the set of non-linear equations. This quick convergence is possible due to the availability of analytic Jacobians. Figure A1 illustrates the quadratic convergence by plotting the residue in the k+1th iteration r_{k+1} versus the residue in the kth iteration r_k (with $r_k = |\mathbf{f_k}|$, as in Section 2.2). Quadratic convergence implies $r_{k+1} \sim r_k^2$. The superimposed trend line r_k^2 shows that the series of residues indeed features quadratic convergence. The left panel in Figure A1 corresponds to the solution of ψ and T_e with the simple ad-hoc transport formula discussed in Section 2.1, while the right panel in Figure A1 corresponds to the solution of ψ, T_e and T_i with a neural network emulation of the stiff quasi-linear gyrokinetic transport model QuaLiKiz (QLKNN-hyper-10D).

Appendix B. Mathematical formulation of a constrained, non-linear parameter optimization problem

Consider a parameter optimization problem with a cost function J, which can contain terms depending on the plasma stationary state vector $\mathbf{x_{SS}}$, its time derivative $\dot{\mathbf{x}}_{\mathbf{SS}}$ and the actuator

vector $\mathbf{u_{SS}}$ (B.1a). The vector $\mathbf{p}$ contains the optimization variables, parametrizing the actuator commands, while the vector $\mathbf{z}$ contains the unknowns parametrizing the stationary solution (as defined in Section 2.2). By defining a matrix $\mathbf{A_{ineq}}$ and a vector $\mathbf{b_{ineq}}$, a set of linear limits on the optimization variables can be imposed (B.1b), for example constraining the total available auxiliary heating power. Furthermore, one can impose a set of non-linear bounds with dependencies on the plasma state, the plasma state derivative and the actuator vector (B.1c). The plasma state dependent constraint functions are formulated as the radial integration of the constraint violation. This approach is further elaborated in [4]. Finally, accordance of the optimal state to the stationary state equation (12) is imposed in (B.1d):

$$\min_{\mathbf{p}} \quad J(\dot{\mathbf{x}}_{\mathbf{SS}}(\mathbf{z}), \mathbf{x}_{\mathbf{SS}}(\mathbf{z}), \mathbf{u}_{\mathbf{SS}}(\mathbf{z}, \mathbf{p})) \tag{B.1a}$$

$$\text{subject to} \quad \mathbf{A_{ineq}}\mathbf{p} \leq \mathbf{b_{ineq}} \tag{B.1b}$$

$$\mathscr{C}(\mathbf{x}_{\mathbf{SS}}(\mathbf{z}), \mathbf{x}_{\mathbf{SS}}(\mathbf{z}), \mathbf{u}_{\mathbf{SS}}(\mathbf{z}, \mathbf{p})) \leq 0 \tag{B.1c}$$

$$\mathbf{f}(\dot{\mathbf{x}}_{\mathbf{SS}}(\mathbf{z}), \mathbf{x}_{\mathbf{SS}}(\mathbf{z}), \mathbf{u}_{\mathbf{SS}}(\mathbf{z}, \mathbf{p})) = 0 \tag{B.1d}$$

A solution to a constrained, non-linear optimization problem like (B.1a)-(B.1d) can be pursued iteratively, applying a non-linear programming solver, starting from an initial guess for the optimization variable $\mathbf{p_0}$. The following steps are repeated until the necessary conditions for optimality, i.e. the Karush-Kuhn-Tucker equations [72], are fulfilled.

- For a given optimization vector $\mathbf{p_i}$, apply the Newton-Raphson solver presented in the previous section to find the stationary solution $\mathbf{z_i}$ of the state equation (B.1d).
- Evaluate $J(\dot{\mathbf{x}}(\mathbf{z_i}), \mathbf{x}(\mathbf{z_i}), \mathbf{u}(\mathbf{z_i}, \mathbf{p_i}))$ and

  $$\frac{\partial J}{\partial \mathbf{p}} = \left[\frac{\partial J}{\partial \dot{\mathbf{x}}}\frac{\partial \dot{\mathbf{x}}}{\partial \mathbf{z}} + \frac{\partial J}{\partial \mathbf{x}}\frac{\partial \mathbf{x}}{\partial \mathbf{z}} + \frac{\partial J}{\partial \mathbf{u}}\frac{\partial \mathbf{u}}{\partial \mathbf{z}}\right]\frac{\partial \mathbf{z}}{\partial \mathbf{p}} + \frac{\partial J}{\partial \mathbf{u}}\frac{\partial \mathbf{u}}{\partial \mathbf{p}} \tag{B.2}$$

  and similarly for the non-linear constraints: evaluate $\mathscr{C}(\dot{\mathbf{x}}(\mathbf{z_i}), \mathbf{x}(\mathbf{z_i}), \mathbf{u}(\mathbf{z_i}, \mathbf{p_i}))$ and $\frac{\partial \mathscr{C}}{\partial \mathbf{p}}$. Note that $\partial \mathbf{z}/\partial \mathbf{p}$ can be obtained by extracting the Jacobian $\partial \mathbf{f}/\partial \mathbf{z}$ at the solution point from the Newton-Raphson solver and by evaluating:

  $$\frac{\partial \mathbf{z}}{\partial \mathbf{p}} = -\left[\frac{\partial \mathbf{f}}{\partial \mathbf{z}}\right]^{-1}\frac{\partial \mathbf{f}}{\partial \mathbf{u}}\frac{\partial \mathbf{u}}{\partial \mathbf{p}} \tag{B.3}$$

  Equation (B.3) effectively imposes the stationarity constraint, restricting the optimization space gradients to the direction maintaining the evaluation of state equation (B.1d) linearly constant, by imposing $\frac{\partial \mathbf{f}}{\partial \mathbf{p}} = 0$.
- J, $\mathscr{C}$, $\frac{\partial J}{\partial \mathbf{p}}$ and $\frac{\partial \mathscr{C}}{\partial \mathbf{p}}$ are provided to a non-linear programming algorithm implemented in the fmincon function of Matlab. For all results presented in this paper, the sequential quadratic programming (SQP) algorithm [72] is used. The SQP algorithm constructs a sequence of quadratic sub-problems, locally approximating the non-linear problem (B.1a)-(B.1d) with a quadratic cost function and linear constraints. By providing gradient information of cost and constraints and applying a quasi-Newton method to approximate the Hessian, these sub-problems are cheaply constructed. The optima of the sub-problems approach the optimum of the original non-linear problem by passing through a set of iterations.

Since we are solving a nonlinear optimization problem, there is no general guarantee of finding a global minimum. Therefore, initiating the optimization routine from different, randomly assigned, initial optimization vectors $\mathbf{p_0}$, confidence can be augmented that the obtained stationary solution is globally optimal. The optimization space gradients required by

the non-linear programming solver are evaluated analytically. This avoids the need for a finite difference approach, which would increase the computational cost by requiring additional stationary state evaluations for each dimension of **p**.

Acknowledgments

This work has been carried out within the framework of the EUROfusion Consortium and has received funding from the Euratom research and training programme 2014 - 2018 and 2019 - 2020 under grant agreement No 633053. The views and opinions expressed herein do not necessarily reflect those of the European Commission. This work is supported in part by the Swiss National Science Foundation.

[1] E Witrant, E Joffrin, S Brémond, G Giruzzi, D Mazon, O Barana, and P Moreau. A control-oriented model of the current profile in tokamak plasma. *Plasma Physics and Controlled Fusion*, 49(7):1075, 2007.

[2] D Humphreys, G Ambrosino, P de Vries, F Felici, S H Kim, G Jackson, A Kallenbach, E Kolemen, J Lister, D Moreau, A Pironti, G Raupp, O Sauter, E Schuster, J Snipes, W Treutterer, M Walker, A Welander, A Winter, and L Zabeo. Novel aspects of plasma control in iter. *Physics of Plasmas*, 22(2):021806, 2015.

[3] F Felici, O Sauter, S Coda, B P Duval, T.P. Goodman, J-M Moret, and J I Paley. Real-time physics-model-based simulation of the current density profile in tokamak plasmas. *Nuclear Fusion*, 51(8):083052, 2011.

[4] F Felici and O Sauter. Non-linear model-based optimization of actuator trajectories for tokamak plasma profile control. *Plasma Physics and Controlled Fusion*, 54(2):025002, 2012.

[5] J van Dongen, F Felici, G M D Hogeweij, P Geelen, and E Maljaars. Numerical optimization of actuator trajectories for ITER hybrid scenario profile evolution. *Plasma Physics and Controlled Fusion*, 56(12):125008, 2014.

[6] A A Teplukhina, O Sauter, F Felici, A Merle, and D Kim. Simulation of profile evolution from ramp-up to ramp-down and optimization of tokamak plasma termination with the RAPTOR code. *Plasma Physics and Controlled Fusion*, 59(12):124004, 2017.

[7] J F Artaud, F Imbeaux, J Garcia, G Giruzzi, T Aniel, V Basiuk, A Bécoulet, C Bourdelle, Y Buravand, J Decker, R Dumont, L G Eriksson, X Garbet, R Guirlet, G T Hoang, P Huynh, E Joffrin, X Litaudon, P Maget, D Moreau, R Nouailletas, B Pégourié, Y Peysson, M Schneider, and J Urban. Metis: a fast integrated tokamak modelling tool for scenario design. *Nuclear Fusion*, 58(10):105001, aug 2018.

[8] J E Barton, M D Boyer, W Shi, W P Wehner, E Schuster, J R Ferron, M L Walker, D A Humphreys, T C Luce, F Turco, B G Penaflor, and R D Johnson. Physics-model-based nonlinear actuator trajectory optimization and safety factor profile feedback control for advanced scenario development in DIII-d. *Nuclear Fusion*, 55(9):093005, jul 2015.

[9] E Fable, C Angioni, M Siccinio, and H Zohm. Plasma physics for fusion reactor system codes: Framework and model code. *Fusion Engineering and Design*, 130:131–136, 2018.

[10] K V Ellis, H Lux, E Fable, R Kembleton, and M. Siccinio. The next step in systems modelling: The integration of a simple 1D transport and equilibrium solver. *EPS Conference, Prague (2018)*, 2018.

[11] M Honda and E Narita. Machine-learning assisted steady-state profile predictions using global optimization techniques. *Physics of Plasmas*, 26(10):102307, 2019.

[12] J Citrin, S Breton, F Felici, F Imbeaux, T Aniel, J F Artaud, B Baiocchi, C Bourdelle, Y Camenen, and J Garcia. Real-time capable first principle based modelling of tokamak turbulent transport. *Nuclear Fusion*, 55(9):092001, 2015.

[13] O Meneghini, S P Smith, P B Snyder, G M Staebler, J Candy, E Belli, L Lao, M Kostuk, T Luce, T Luda, J M Park, and F Poli. Self-consistent core-pedestal transport simulations with neural network accelerated models. *Nuclear Fusion*, 57(8):086034, jul 2017.

[14] F Felici, J Citrin, A A Teplukhina, J Redondo, C Bourdelle, F Imbeaux, and O Sauter. Real-time-capable prediction of temperature and density profiles in a tokamak using RAPTOR and a first-principle-based transport model. *Nuclear Fusion*, 58(9):096006, jul 2018.

[15] K L van de Plassche, J Citrin, C Bourdelle, Y Camenen, F J Casson, V I Dagnelie, F Felici, A Ho, and S Van Mulders. Fast modeling of turbulent transport in fusion plasmas using neural networks. *Physics of Plasmas*, 27(2):022310, 2020.

[16] C Bourdelle, J Citrin, B Baiocchi, A Casati, P Cottier, X Garbet, and F Imbeaux. Core turbulent transport in tokamak plasmas: bridging theory and experiment with QuaLiKiz. *Plasma Physics and Controlled Fusion*, 58(1):014036, dec 2015.

[17] J Citrin, C Bourdelle, F J Casson, C Angioni, N Bonanomi, Y Camenen, X Garbet, L Garzotti, T Görler, O Gürcan, F Koechl, F Imbeaux, O Linder, K van de Plassche, P Strand, and G Szepesi. Tractable flux-driven temperature, density, and rotation profile evolution with the quasilinear gyrokinetic transport model QuaLiKiz. *Plasma Physics and Controlled Fusion*, 59(12):124005, nov 2017.

[18] P Mantica, C Angioni, N Bonanomi, J Citrin, B A Grierson, F Koechl, A Mariani, and G M Staebler. Progress and challenges in understanding core transport in tokamaks in support to ITER operations. *Plasma Physics and Controlled Fusion*, 62(1):014021, dec 2019.

[19] J M Park, M. Murakami, H E St. John, L L Lao, M S Chu, and R. Prater. An efficient transport solver for tokamak plasmas. *Computer Physics Communications*, 214:1 – 5, 2017.

[20] G V Pereverzev and G Corrigan. Stable numeric scheme for diffusion equation with a stiff transport. *Computer Physics Communications*, 179(8):579–585, 2008.

[21] J Candy, C Holland, R E Waltz, M R Fahey, and E Belli. Tokamak profile prediction using direct gyrokinetic and neoclassical simulation. *Physics of Plasmas*, 16(6):060704, 2009.

[22] ITER Physics Basis Expert Groups on Confinement and Transport and Confinement Modelling and Database, ITER Physics Basis Editors. Chapter 2: Plasma confinement and transport. *Nuclear Fusion*, 39(12):2175, dec 1999.

[23] F Wagner, A Becoulet, R Budny, V Erckmann, D Farina, G Giruzzi, Y Kamada, A Kaye, F Koechl, K Lackner, N Marushchenko, M Murakami, T Oikawa, V Parail, J M Park, G Ramponi, O Sauter, D Stork, P R Thomas, Q M Tran, D Ward, H Zohm, and C Zucca. On the heating mix of ITER. *Plasma Physics and Controlled Fusion*, 52(12):124044, nov 2010.

[24] J Citrin, J-F Artaud, J Garcia, G M D Hogeweij, and F Imbeaux. Impact of heating and current drive mix on the ITER hybrid scenario. *Nuclear Fusion*, 50(11):115007, oct 2010.

[25] A R Polevoi, A A Ivanov, S Yu Medvedev, G T A Huijsmans, S H Kim, A Loarte, E Fable, and A Y Kuyanov. Reassessment of steady-state operation in ITER with NBI and EC heating and current drive. *Nuclear Fusion*, 60(9):096024, aug 2020.

[26] W P Wehner, E Schuster, M D Boyer, and F M Poli. Transp-based optimization towards tokamak scenario development. *Fusion Engineering and Design*, 146:547–550, 2019. SI:SOFT-30.

[27] J McClenaghan, A M Garofalo, L L Lao, D B Weisberg, O Meneghini, S P Smith, B C Lyons, G M Staebler, S Y Ding, J Huang, X Gong, J Qian, Q Ren, and C T Holcomb. Transport at high β_p and development of candidate steady state scenarios for ITER. *Nuclear Fusion*, 60(4):046025, mar 2020.

[28] S H Kim, A R Polevoi, A Loarte, S Yu Medvedev, and G Huijsmans. A study of the heating and current drive options and confinement requirements to access steady-state plasmas at q~5 in ITER and associated operational scenario development. *Nuclear Fusion*, apr 2021.

[29] N Hayashi, J Garcia, M Honda, E Narita, S Ide, G Giruzzi, and Y Sakamoto. Transport modelling of JT-60u and JET plasmas with internal transport barriers towards prediction of JT-60sa high-beta steady-state scenario. *Nuclear Fusion*, 57(12):126037, oct 2017.

[30] P Rodriguez-Fernandez, N T Howard, M J Greenwald, A J Creely, J W Hughes, J C Wright, C Holland, Y Lin, and F Sciortino. Predictions of core plasma performance for the sparc tokamak. *Journal of Plasma Physics*, 86(5):865860503, 2020.

[31] O Sauter, C Angioni, and Y R Lin-Liu. Neoclassical conductivity and bootstrap current formulas for general axisymmetric equilibria and arbitrary collisionality regime. *Physics of Plasmas*, 6(7):2834–2839, 1999.

[32] O Sauter, C Angioni, and Y R Lin-Liu. Erratum: "neoclassical conductivity and bootstrap current formulas for general axisymmetric equilibria and arbitrary collisionality regime" [phys. plasmas 6, 2834 (1999)]. *Physics of Plasmas*, 9(12):5140–5140, 2002.

[33] C D Challis, J G Cordey, H Hamnén, P M Stubberfield, J P Christiansen, E Lazzaro, D G Muir, D Stork, and E Thompson. Non-inductively driven currents in JET. *Nuclear Fusion*, 29(4):563–570, apr 1989.

[34] G Cenacchi and A Taroni. Jetto a free boundary plasma transport code. *ENEA-RT-TIB–88-5*, 1988.

[35] O Sauter, S Coda, T P Goodman, M A Henderson, R Behn, A Bottino, E Fable, An Martynov, P Nikkola, and C Zucca. Inductive current density perturbations to probe electron internal transport barriers in tokamaks. *Physical Review Letters*, 94:105002, Mar 2005.

[36] C Zucca, O Sauter, E Asp, S Coda, E Fable, T P Goodman, and M A Henderson. Current density evolution in electron internal transport barrier discharges in TCV. *Plasma Physics and Controlled Fusion*, 51(1):015002, dec 2008.

[37] O Sauter, M A Henderson, F Hofmann, T Goodman, S Alberti, C Angioni, K Appert, R Behn, P Blanchard, P Bosshard, R Chavan, S Coda, B P Duval, D Fasel, A Favre, I Furno, P Gorgerat, J-P Hogge, P-F Isoz, B Joye, P Lavanchy, J B Lister, X Llobet, J-C Magnin, P Mandrin, A Manini, B Marlétaz, P Marmillod, Y Martin, J-M Mayor, A A Martynov, J Mlynar, J-M Moret, C Nieswand, P Nikkola, P Paris, A Perez, Z A Pietrzyk, R A Pitts, A Pochelon, G Pochon, A Refke, H Reimerdes, J Rommers, E Scavino, G Tonetti, M Q Tran, F Troyon, and H Weisen. Steady-state fully noninductive current driven by electron cyclotron waves in a magnetically confined plasma. *Physical Review Letters*, 84:3322–3325, Apr 2000.

[38] S Coda, T P Goodman, M A Henderson, F Hofmann, Z A Pietrzyk, O Sauter, S Alberti, C Angioni, K Appert, R Behn, P Blanchard, P Bosshard, R Chavan, A Degeling, B P Duval, D Fasel, A Favre, I Furno, P Gomez, P Gorgerat, J-P Hogge, P-F Isoz, B Joye, P Lavanchy, J B Lister, X Llobet, J-C Magnin, A Manini, B Marlétaz, P Marmillod, Y Martin, An Martynov, J-M Mayor, J Mlynar, J-M Moret, P Nikkola, P J Paris, A Perez, Y Peysson, R A Pitts, A Pochelon, H Reimerdes, J H Rommers, E Scavino, A Sushkov, G Tonetti,

M Q Tran, H Weisen, and A Zabolotsky. High-power ECH and fully non-inductive operation with ECCD in the TCV tokamak. *Plasma Physics and Controlled Fusion*, 42(12B):B311–B321, dec 2000.

[39] O Sauter, C Angioni, S Coda, P Gomez, T P Goodman, M A Henderson, F Hofmann, J-P Hogge, J-M Moret, P Nikkola, Z A Pietrzyk, H Weisen, S Alberti, K Appert, J Bakos, R Behn, P Blanchard, P Bosshard, R Chavan, I Condrea, A Degeling, B P Duval, D Fasel, J-Y Favez, A Favre, I Furno, R R Kayruthdinov, P Lavanchy, J B Lister, X Llobet, V E Lukash, P Gorgerat, P-F Isoz, B Joye, J-C Magnin, A Manini, B Marlétaz, P Marmillod, Y R Martin, An Martynov, J-M Mayor, E Minardi, J Mlynar, P J Paris, A Perez, Y Peysson, V Piffl, R A Pitts, A Pochelon, H Reimerdes, J H Rommers, E Scavino, A Sushkov, G Tonetti, M Q Tran, and A Zabolotsky. Steady-state fully noninductive operation with electron cyclotron current drive and current profile control in the tokamak à configuration variable (tcv). *Physics of Plasmas*, 8(5):2199–2207, 2001.

[40] A Gude, S Günter, and S Sesnic. Seed island of neoclassical tearing modes at ASDEX upgrade. *Nuclear Fusion*, 39(1):127–131, jan 1999.

[41] ITER Organization. *ITER Research Plan within the Staged Approach (Level III – Provisional Version)*. ITER technical report ITR-18-003, 2018.

[42] M Greenwald, J L Terry, S M Wolfe, S Ejima, M G Bell, S M Kaye, and G H Neilson. A new look at density limits in tokamaks. *Nuclear Fusion*, 28(12):2199–2207, dec 1988.

[43] G. Verdoolaege, S.M. Kaye, C. Angioni, O.J.W.F. Kardaun, M. Maslov, M. Romanelli, F. Ryter, K. Thomsen, the ASDEX Upgrade Team, the EUROfusion MST1 Team, and JET Contributors. The updated ITPA global h-mode confinement database: description and analysis. *Nuclear Fusion*, 61(7):076006, may 2021.

[44] M Shimada, D J Campbell, V Mukhovatov, M Fujiwara, N Kirneva, K Lackner, M Nagami, V D Pustovitov, N Uckan, J Wesley, N Asakura, A E Costley, A J H Donné, E J Doyle, A Fasoli, C Gormezano, Y Gribov, O Gruber, T C Hender, W Houlberg, S Ide, Y Kamada, A Leonard, B Lipschultz, A Loarte, K Miyamoto, V Mukhovatov, T H Osborne, A Polevoi, and A C C Sips. Chapter 1: Overview and summary. *Nuclear Fusion*, 47(6):S1–S17, jun 2007.

[45] M Kong, T C Blanken, F Felici, C Galperti, E Maljaars, O Sauter, T Vu, F Carpanese, A Merle, J-M Moret, F Pesamosca, E Poli, M Reich, and A A Teplukhina. Control of neoclassical tearing modes and integrated multi-actuator plasma control on TCV. *Nuclear Fusion*, 59(7):076035, jun 2019.

[46] J Stober, A C C Sips, C Angioni, C B Forest, O Gruber, J Hobirk, L D Horton, C F Maggi, M Maraschek, P Martin, P J Mc Carthy, V Mertens, Y-S Na, M Reich, A Staebler, G Tardini, and H Zohm. The role of the current profile in the improved h-mode scenario in ASDEX upgrade. *Nuclear Fusion*, 47(8):728–737, jul 2007.

[47] J Citrin, J Hobirk, M Schneider, J F Artaud, C Bourdelle, K Crombe, G M D Hogeweij, F Imbeaux, E Joffrin, F Koechl, and J Stober. Predictive analysis of q-profile influence on transport in JET and ASDEX upgrade hybrid scenarios. *Plasma Physics and Controlled Fusion*, 54(6):065008, may 2012.

[48] G M D Hogeweij, J-F Artaud, T A Casper, J Citrin, F Imbeaux, F Koechl, X Litaudon, and I Voitsekhovitch. Optimizing the current ramp-up phase for the hybrid ITER scenario. *Nuclear Fusion*, 53(1):013008, dec 2012.

[49] J Citrin, J Garcia, T Goerler, F Jenko, P Mantica, D Told, C Bourdelle, D R Hatch, G M D Hogeweij, T Johnson, M J Pueschel, and M Schneider. Electromagnetic stabilization of tokamak microturbulence in a high-β regime. *Plasma Physics and Controlled Fusion*, 57(1):014032, nov 2014.

[50] J Garcia, T Goerler, and F Jenko. Isotope and fast ions turbulence suppression effects: Consequences for high-β iter plasmas. *Physics of Plasmas*, 25(5):055902, 2018.

[51] A R Polevoi, A Loarte, N Hayashi, H S Kim, S H Kim, F Koechl, A S Kukushkin, V M Leonov, S Yu Medvedev, M Murakami, Y S Na, A Y Pankin, J M Park, P B Snyder, J A Snipes, and V E Zhogolev. Assessment of operational space for long-pulse scenarios in ITER. *Nuclear Fusion*, 55(6):063019, may 2015.

[52] E Fable, C Angioni, V Bobkov, J Stober, R Bilato, G D Conway, T Goerler, R M McDermott, T Puetterich, M Siccinio, W Suttrop, M Teschke, and H Zohm. The role of the source versus the collisionality in predicting a reactor density profile as observed on ASDEX upgrade discharges. *Nuclear Fusion*, 59(7):076042, jun 2019.

[53] C Angioni, A G Peeters, G V Pereverzev, F Ryter, and G Tardini. Density peaking, anomalous pinch, and collisionality in tokamak plasmas. *Physical Review Letters*, 90:205003, May 2003.

[54] H Weisen, A Zabolotsky, C Angioni, I Furno, X Garbet, C Giroud, H Leggate, P Mantica, D Mazon, J Weiland, L Zabeo, and K.-D Zastrow. Collisionality and shear dependences of density peaking in JET and extrapolation to ITER. *Nuclear Fusion*, 45(2):L1–L4, jan 2005.

[55] Martin Greenwald. Density limits in toroidal plasmas. *Plasma Physics and Controlled Fusion*, 44(8):R27–R53, jul 2002.

[56] T Eich, R J Goldston, A Kallenbach, B Sieglin, and H J Sun. Correlation of the tokamak h-mode density limit with ballooning stability at the separatrix. *Nuclear Fusion*, 58(3):034001, jan 2018.

[57] H Lütjens, A Bondeson, and O Sauter. The chease code for toroidal mhd equilibria. *Computer Physics Communications*, 97(3):219–260, 1996.

[58] F Koechl, S D Pinches, F J Casson, J Citrin, G Corrigan, M Dubrov, Y Gribov, D Harting, A A Kavin, R R Khayrutdinov, S-H Kim, P J Knight, S V Konovalov, A Loarte, V E Lukash, M Marin, S Medvedev, V Parail, A R Polevoi, and M Romanelli. Optimising the ITER 15 MA DT baseline scenario by exploiting a self-consistent free-boundary core-edge-SOL workflow in IMAS. *Preprint: 2018 IAEA Fusion Energy Conference, Gandhinagar*.

[59] T C Luce, Y R Lin-Liu, R W Harvey, G Giruzzi, P A Politzer, B W Rice, J M Lohr, C C Petty, and R Prater. Generation of localized noninductive current by electron cyclotron waves on the diii-d tokamak. *Physical Review Letters*, 83:4550–4553, Nov 1999.

[60] Y R Lin-Liu, V S Chan, and R Prater. Electron cyclotron current drive efficiency in general tokamak geometry. *Physics of Plasmas*, 10(10):4064–4071, 2003.

[61] E Fable, C Angioni, and O Sauter. The role of ion and electron electrostatic turbulence in characterizing stationary particle transport in the core of tokamak plasmas. *Plasma Physics and Controlled Fusion*, 52(1):015007, dec 2009.

[62] N Kumar, Y Camenen, S Benkadda, C Bourdelle, A Loarte, A R Polevoi, and F Widmer. Turbulent transport driven by kinetic ballooning modes in the inner core of JET hybrid h-modes. *Nuclear Fusion*, 61(3):036005, dec 2020.

[63] X Jian, V S Chan, J Chen, A Bock, H Zohm, E Fable, M Reisner, W Guo, and G Zhuang. Key effects on the confinement improvement of the ASDEX upgrade hybrid scenario. *Nuclear Fusion*, 59(10):106038, sep 2019.

[64] S Mazzi, J Garcia, D Zarzoso, Ye O Kazakov, J Ongena, M Nocente, M Dreval, Z Stancar, G Szepesi, J Eriksson, A Sahlberg, and S Benkadda. Towards enhanced performance in fusion plasmas via turbulence suppression by MeV ions. *arXiv:2010.07977, submittted to Nature Physics*, 2020.

[65] J Stober, F Sommer, C Angioni, A Bock, E Fable, F Leuterer, F Monaco, S Müller, M Münich, B Petzold, E Poli, M Schubert, H Schütz, D Wagner, H Zohm, W Kasparek, B Plaum, A Meier, Th Scherer, D Strauss, J Jelonnek, M Thumm, A Litvak, G G Denisov, A V Chirkov, E M Tai, L G Popov, V O Nichiporenko, V E Myasnikov, E A Soluyanova, and V Malygin. High power ecrh and eccd in moderately collisional asdex upgrade h- modes and status of ec system upgrade. *EPJ Web of Conferences*, 87:02004, 2015.

[66] Y R Martin and T Takizuka. Power requirement for accessing the h-mode in ITER. *Journal of Physics: Conference Series*, 123:012033, jul 2008.

[67] R J Dumont and D Zarzoso. Heating and current drive by ion cyclotron waves in the activated phase of ITER. *Nuclear Fusion*, 53(1):013002, dec 2012.

[68] P T Lang, W Suttrop, E Belonohy, M Bernert, R M Mc Dermott, R Fischer, J Hobirk, O J W F Kardaun, G Kocsis, B Kurzan, M Maraschek, P de Marne, A Mlynek, P A Schneider, J Schweinzer, J Stober, T Szepesi, K Thomsen, W Treutterer, and E Wolfrum. High-density h-mode operation by pellet injection and ELM mitigation with the new active in-vessel saddle coils in ASDEX upgrade. *Nuclear Fusion*, 52(2):023017, jan 2012.

[69] T Hein, C Angioni, E Fable, and J Candy. Gyrokinetic study of the role of $\hat{I}^2$ on electron particle transport in tokamaks. *Physics of Plasmas*, 17(10):102309, 2010.

[70] P Horn. *Inclusion of physics constraints in neural network surrogate models for fusion simulation*. Master Thesis, Technische Universiteit Eindhoven, 2020.

[71] M Weiland, R Bilato, R Dux, B Geiger, A Lebschy, F Felici, R Fischer, D Rittich, and M van Zeeland. RABBIT: Real-time simulation of the NBI fast-ion distribution. *Nuclear Fusion*, 58(8):082032, jul 2018.

[72] J Nocedal and S J Wright. *Numerical Optimization*. Springer, second edition, 2006.